Cell Reports

Article

Germline-specific RNA helicase DDX4 forms cytoplasmic granules in cancer cells and promotes tumor growth

Graphical abstract

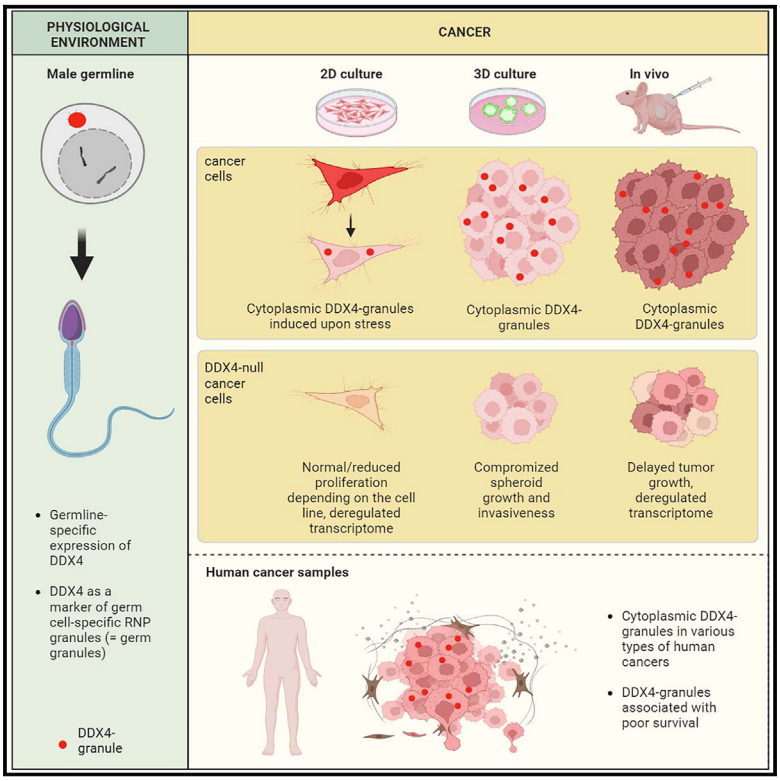

Highlights

- Germ-granule-resembling DDX4 granules appear in different somatic malignancies
- Deletion of *DDX4* in cancer cells compromises tumor growth
- *DDX4* deletion affects the expression of genes associated with cancer invasiveness
- DDX4 expression is associated with poor survival of cancer patients

Authors

Opeyemi Olotu, Anna-Riina Koskenniemi, Lin Ma, ..., Paula Vainio, Juho-Antti Mäkelä, Noora Kotaja

Correspondence

noora.kotaja@utu.fi

In brief

Olotu et al. reveal the presence of cytoplasmic granules containing the germline-specific RNA helicase DDX4 in various human cancers. Using cultured cancer cells and a mouse xenograft model, they show that DDX4 is involved in the transcriptome regulation in cancer cells, and it promotes cancerous properties and tumor growth.

Olotu et al., 2024, Cell Reports *43*, 114430
July 23, 2024 © 2024 The Author(s). Published by Elsevier Inc.
https://doi.org/10.1016/j.celrep.2024.114430

CellPress

Cell Reports

CellPress
OPEN ACCESS

Article

Germline-specific RNA helicase DDX4 forms cytoplasmic granules in cancer cells and promotes tumor growth

Opeyemi Olotu,[1] Anna-Riina Koskenniemi,[2] Lin Ma,[1] Valeriy Paramonov,[1,3,4] Sini Laasanen,[1] Elina Louramo,[1] Matthieu Bourgery,[1,5] Tiina Lehtiniemi,[1] Samuli Laasanen,[1] Adolfo Rivero-Müller,[6] Eliisa Löyttyniemi,[7] Cecilia Sahlgren,[3,4] Jukka Westermarck,[1,4] Sami Ventelä,[4,8] Tapio Visakorpi,[9,10] Matti Poutanen,[1,11,12] Paula Vainio,[2] Juho-Antti Mäkelä,[1] and Noora Kotaja[1,13,*]

[1]Institute of Biomedicine, Integrative Physiology and Pharmacology Unit, University of Turku, 20520 Turku, Finland
[2]Department of Pathology, Laboratory Division, Turku University Hospital and University of Turku, 20520 Turku, Finland
[3]Faculty of Science and Engineering, Cell Biology, Åbo Akademi University, 20500 Turku, Finland
[4]Turku Bioscience, University of Turku and Åbo Akademi University, 20520 Turku, Finland
[5]Centre for Population Health Research, Turku University Hospital and University of Turku, 20520 Turku, Finland
[6]Department of Biochemistry and Molecular Biology, Medical University of Lublin, 20-093 Lublin, Poland
[7]Department of Biostatistics, University of Turku and Turku University Hospital, 20520 Turku, Finland
[8]Department for Otorhinolaryngology, Head, and Neck Surgery, University of Turku and Turku University Hospital, 20520 Turku, Finland
[9]Faculty of Medicine and Health Technology, Tampere University and Tays Cancer Center, Tampere University Hospital, 33520 Tampere, Finland
[10]Fimlab Laboratories, Tampere University Hospital, 33520 Tampere, Finland
[11]Turku Center for Disease Modeling, University of Turku, 20520 Turku, Finland
[12]FICAN West Cancer Center, University of Turku, Turku University Hospital, 20500 Turku, Finland
[13]Lead contact
*Correspondence: noora.kotaja@utu.fi
https://doi.org/10.1016/j.celrep.2024.114430

SUMMARY

Cancer cells undergo major epigenetic alterations and transcriptomic changes, including ectopic expression of tissue- and cell-type-specific genes. Here, we show that the germline-specific RNA helicase DDX4 forms germ-granule-like cytoplasmic ribonucleoprotein granules in various human tumors, but not in cultured cancer cells. These cancerous DDX4 complexes contain RNA-binding proteins and splicing regulators, including many known germ granule components. The deletion of *DDX4* in cancer cells induces transcriptomic changes and affects the alternative splicing landscape of a number of genes involved in cancer growth and invasiveness, leading to compromised capability of *DDX4*-null cancer cells to form xenograft tumors in immunocompromised mice. Importantly, the occurrence of DDX4 granules is associated with poor survival in patients with head and neck squamous cell carcinoma and higher histological grade of prostate cancer. Taken together, these results show that the germ-granule-resembling cancerous DDX4 granules control gene expression and promote malignant and invasive properties of cancer cells.

INTRODUCTION

Cancer formation and progression are dictated by an accumulation of somatic mutations, epigenetic mutations, and transcriptomic alterations. Cancer cells have an exceptional quality to reprogram their epigenome to promote cell growth and survival, leading to the aberrant expression of genes that are not normally expressed in the tissue and cell type from which the cancer cells originate.[1] In addition to somatic genes, many germline-specific genes, known as cancer-germline antigens (CGAs), are misexpressed in cancer.[2] Systematic analysis revealed more than 1,000 CGA genes that are ectopically expressed in different somatic malignancies.[3] CGA genes have been suggested to support tumor formation by promoting oncogenic processes or evading the functions of tumor suppressors, and their expression is often associated with poor clinical outcomes.[4] CGAs are potential targets for cancer immunotherapies such as cancer vaccines and autologous T cells.[5]

The extensive transcriptomic alterations in cancer cells are posttranscriptionally controlled by a variety of RNA-binding proteins that form ribonucleoprotein (RNP) complexes with different species of RNA.[6] Dysregulated expression and function of RNA-binding proteins can serve as mechanistic drivers for several cancer hallmarks.[7,8] Therefore, the chemical modulation of RNA-binding proteins to disrupt their function provides a promising approach to impair cancer cell fitness and improve therapy response.[7] RNP complexes can form larger cytoplasmic RNP granules, which function as platforms for distinct

This is an open access article under the CC BY license (http://creativecommons.org/licenses/by/4.0/).

posttranscriptional regulatory mechanisms to enable coordinated transcriptome regulation.[9] In cancer cells, increased transcriptome complexity induce the formation of RNP granules, such as stress granules and processing bodies, which enhance cancer cell adaptability during tumor formation, progression, and metastasis.[10]

RNP granules also abound in male germ cells. The two most prominent germline-specific RNP granules (germ granules) are the intermitochondrial cement and the chromatoid body (CB), which appear in the cytoplasm of differentiating male germ cells during spermatogenesis.[11] Germ granules resemble processing bodies and stress granules, but contain several germ cell-specific components, and many of their functions are therefore restricted to the germ line.[12] In particular, germ granules are implicated as platforms for the processing and function of PIWI-interacting RNAs (piRNAs), the germline-expressed small non-coding RNAs.[11,13] In mammalian germ granules, the piRNA pathway integrates with other RNA regulatory pathways to support sperm production and male fertility.[14]

A highly conserved ATP-dependent RNA-helicase DDX4 (DEAD-box helicase 4) is considered an archetypical marker of germ granules.[15–17] It is highly abundant in the CB of mouse haploid spermatids[13] and also forms cytoplasmic granules in human round spermatids.[14] DDX4 is essential for germline function, and its genetic ablation leads to sexually dimorphic germline defects across a number of species.[15] In mice, *Ddx4* deletion results in an arrest of spermatogenesis at the zygotene phase of the meiotic prophase I and male infertility.[18,19]

Many CGAs are involved in RNA regulatory processes, but the function of germ granule components and germ-granule-like structures in cancer has remained uncharacterized. Here, we reveal the presence of germ-granule-like cytoplasmic RNA regulatory structures in cancer cells using a germ granule marker, DDX4. Our data show that DDX4-mediated RNA regulation is important for tumor growth and invasiveness. We also highlight the prognostic value of DDX4 in human prostate cancer (PC) and head and neck squamous cell carcinoma (HNSCC).

RESULTS

Germ granule component DDX4 forms cytoplasmic granules in cancer cells

To address the involvement of germ-granule-associated proteins in cancer, we compared a published list of CGAs[3] to the 88 proteins we previously identified as CB components[13] and found an overlap of 22 proteins (25%) (Figure 1A). One of the proteins was DDX4. Due to the well-established role of DDX4 as a key germ granule component,[15] we performed immunostaining with an antibody against DDX4 on a tumor microarray (TMA) containing different human cancers as well as normal tissues to explore the presence of germ granules. No DDX4 signal was observed in normal human somatic tissues, including the breast, colon, and lung (Figure 1B). However, many somatic malignancies presented with a clear DDX4^{+} signal, as exemplified by adenocarcinomas of the breast, colon, and lung (Figure 1B). Cancerous DDX4 localization appeared cytoplasmic, and similar to the male germ line, the signal accumulated in prominent granules (Figure 1B). The presence of DDX4 granules was not restricted to epithelial cancers (carcinomas), but different mesenchymal malignancies (sarcomas) were also found to be positive for DDX4, indicating a more generalized expression of DDX4 in many types of cancers (Figure 1C).

DDX4 forms granules only in the tumor microenvironment

To study whether DDX4 granules are also present in cancer cell lines, we performed immunostaining of human PC3 cells, which are derived from PC metastasis, and University of Turku-squamous cell carcinoma-14 (UT-SCC-14) cells, which are derived from HNSCC.[20–22] We either cultured the cells as a monolayer or inoculated them subcutaneously in immunocompromised mice to induce xenograft tumors. To obtain comparable samples, we embedded both cultured cell pellets and dissected tumors in paraffin for sectioning and immunostaining. DDX4 granules were prominent in solid UT-SCC-14 xenograft tumors, as detected by both immunohistochemistry (Figure 2A) and immunofluorescence (Figure 2B). However, although a weak cytoplasmic DDX4 signal was also observed in the HNSCC cells cultured as a monolayer, no granular signal was detected (Figure 2B). Similarly, DDX4 granules were detected in PC3 xenograft tumors but not in monolayer-cultured PC3 cells (Figure 2C). Western blot analysis of DDX4 enriched by immunoprecipitation showed higher expression of full-length DDX4 (79 kDa) in PC3 tumor extracts compared to monolayer-grown PC3 cells (Figure 2D). Notably, the formation of DDX4 granules was detected in PC3-cell-derived spheroids cultured in 3-dimensional (3D)-Matrigel, an environment that mimics the *in vivo* tumor environment (Figure 2E). Therefore, the germ-granule-like structures only form when cancer cells are in the 3D tumor microenvironment. Interestingly, although DDX4 granules were not detectable in monolayer-cultured PC3 cells, treatment of the cells with the translational inhibitor puromycin induced the formation of prominent granules (Figure 2F). This finding suggests that DDX4 granules are associated with the cellular stress conditions often encountered in oxygen- and nutrient-deprived tumor microenvironments.

DDX4 deletion compromises spheroid formation and invasive properties of cancer cells

To investigate whether DDX4 has a functional role in cancer, we performed a targeted deletion in exon 11 of *DDX4* (hereafter referred to as *DDX4*-null) in PC3 cells using clustered regularly interspaced short palindromic repeats (CRISPR-Cas9) technology. By Sanger sequencing and genomic PCR, 2 mutant *DDX4*-null clones were validated to have the same deletion of 103 nt that caused a frameshift mutation (Figures 3A, 3B, and S1A). *DDX4*-null cells appeared morphologically normal (Figure S1B), and there was no significant difference in the proliferation rates of *DDX4*-null and wild-type (WT) PC3 cells (Figure 3C). Also, the number of apoptotic cells was comparable (Figure 3D).

To study whether the deletion of *DDX4* affects the tumor-forming properties of cancer cells, we performed a 3D organotypic culture. The size of the spheroids formed by *DDX4*-null PC3 cells was significantly smaller already at day 5 compared to WT PC3 cells, and even more pronounced differences were

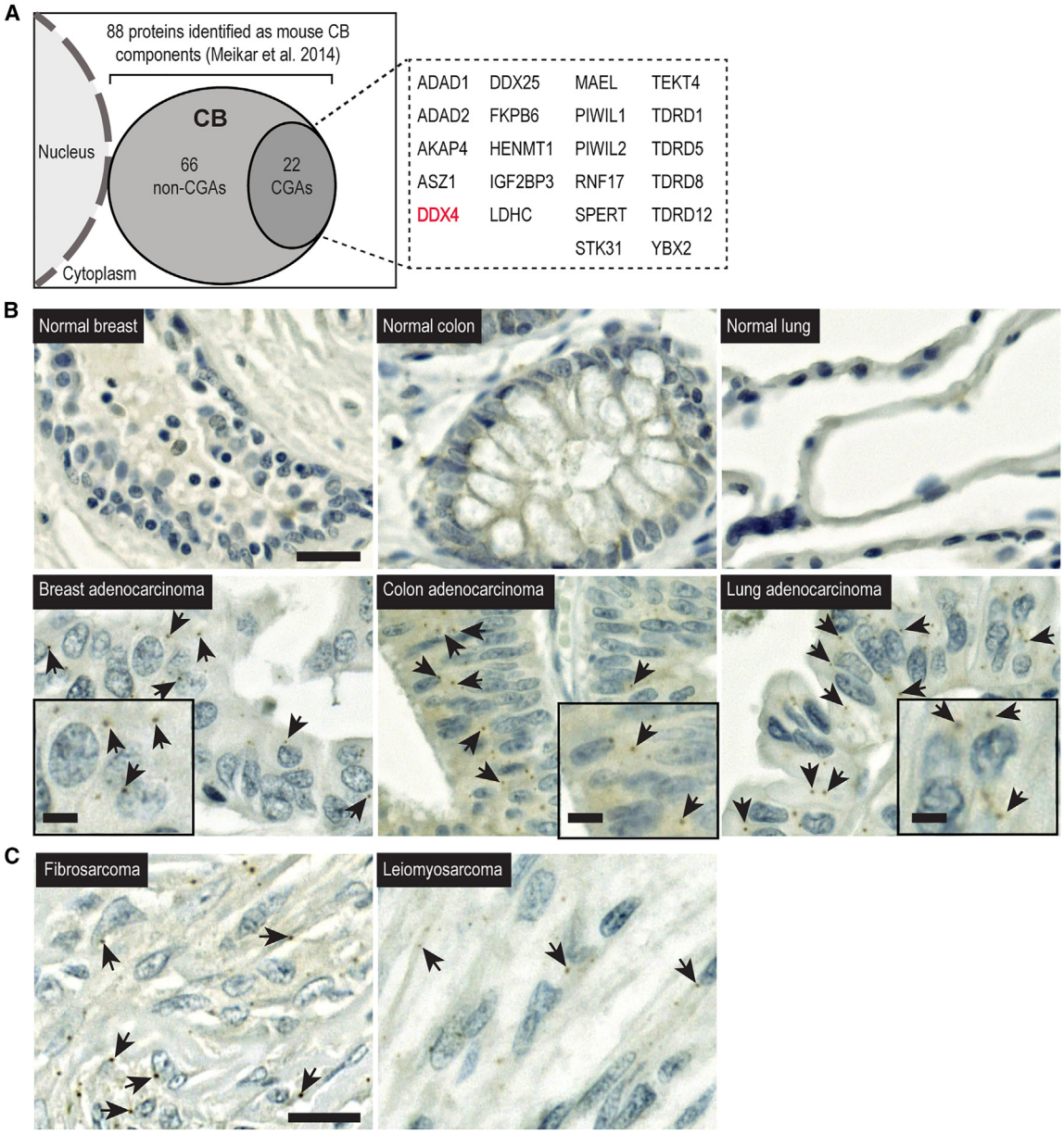

Figure 1. DDX4 forms cytoplasmic granules in cancer cells

(A) Of the 88 known components of the CB, 22 have also been identified as CGAs (the dotted rectangular box, DDX4 highlighted in red).

(B) Immunostaining of different human epithelial tissues with an anti-DDX4 antibody. DDX4 granules are absent from the normal epithelial tissues, but present (black arrows) in the cytoplasm of cancer cells in breast, colon, and lung adenocarcinoma; scale bar: 20 μm. Selected cancer cells are highlighted in the insets; scale bar: 10 μm.

(C) Immunostaining of fibrosarcoma and leiomyosarcoma tissues as examples of DDX4^{+} cancers that are not of epithelial origin. Selected DDX4 granules are indicated with black arrows. Scale bar: 20 μm.

found at day 10 (Figures 3E and 3F), indicating compromised spheroid formation in the absence of DDX4. We then studied the effect of *DDX4* deletion on the invasive properties of PC3 cells and showed that the length of the invasive structures (measured as maxapp index)[23] of spheroids formed by *DDX4*-null PC3 cells was significantly reduced compared to control (Figure 3G). Immunostaining of the spheroids with vimentin, a widely studied marker of invasiveness,[24,25] revealed the disorganization of vimentin in the periphery of *DDX4*-null spheroids (Figure 3H). To study whether the tumor-forming properties of *DDX4*-null PC3 cells can be restored, we performed transient overexpression of DDX4 with a C-terminal GFP tag (DDX4-GFP), and this was able to rescue the phenotype caused by *DDX4* deletion in *DDX4*-null PC3 cells (Figures 3I–3K). Both the size and invasive structures of spheroids formed by DDX4-GFP-overexpressing null cells were

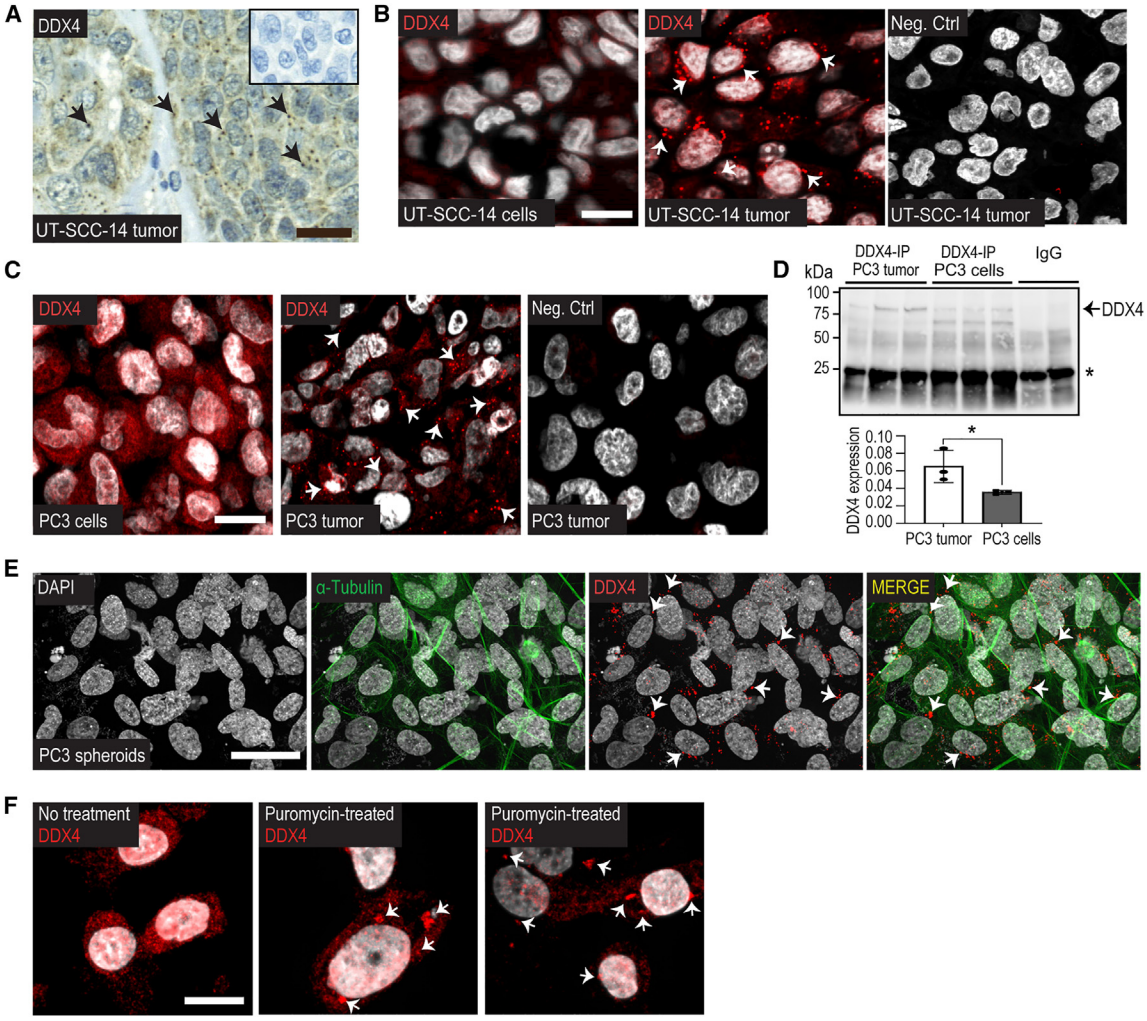

Figure 2. DDX4 granules are found in cancer-cell-line-derived xenograft tumors

(A) Immunohistochemistry of UT-SCC-14-derived xenograft tumors with an anti-DDX4 antibody. Selected DDX4 granules are indicated with black arrows. Scale bar: 20 μm. Smaller rectangular box: no primary antibody control.

(B) Immunofluorescence of UT-SCC-14 cultured cells and tumors with an anti-DDX4 antibody (red), nuclei are stained with DAPI (gray). DDX4 granules (white arrows) appear in xenograft tumor cells. Neg. Ctrl: no primary antibody. Scale bar: 10 μm.

(C) Immunofluorescence of cultured PC3 cells and PC3-derived tumors with an anti-DDX4 antibody (red). DDX4 granules (white arrows) can be detected in tumors. Scale bar: 10 μm.

(D) DDX4 IP from PC3 tumors and cells (3 biological replicates each) followed by western blotting. Rabbit IgG was used as a negative control. Graph: DDX4 signal was quantified, and the signal intensities were normalized to the IgG light-chain signal (asterisk) ($p = 0.0274$, Mann-Whitney U test, 2-tailed).

(E) Immunofluorescence of PC3 spheroids with an anti-DDX4 antibody (red). Anti-α-tubulin antibody (green) visualizes cytoplasmic protrusions. White arrows point to selected DDX4 granules. Scale bar: 20 μm.

(F) Immunofluorescence of DDX4 (red) in non-treated and puromycin-treated PC3 cells. DAPI (gray) stains the nuclei. Scale bar: 10 μm.

significantly increased compared to control GFP-overexpressing null cells (Figures 3J and 3K). Successful overexpression of DDX4 was validated by live-cell microscopy and western blotting (Figure S1C). We also created *DDX4* deletion in an HNSCC cell line, UT-SCC-14 (Figures S1D and S1E), and validated the compromised spheroid growth and formation of protrusions in the absence of functional DDX4 (Figures S2A and S2B). These results suggest that DDX4 promotes cancer cell tumor formation and invasiveness in the 3D *in vitro* environment.

Deletion of *DDX4* causes a delay in tumor formation

We next performed subcutaneous inoculation of WT and *DDX4*-null PC3 cells into athymic nude male mice to study the effects of *DDX4* deletion on xenograft tumor formation and growth *in vivo* for a period of 4 weeks. Weekly measurements of tumor volume revealed that *DDX4*-null PC3 tumors were significantly smaller than WT PC3 tumors at all time points (Figure 4A). The weights of the *DDX4*-null PC3-derived tumors dissected 4 weeks after the inoculation were also significantly decreased compared to the WT PC3-derived tumors (Figure 4B). No significant

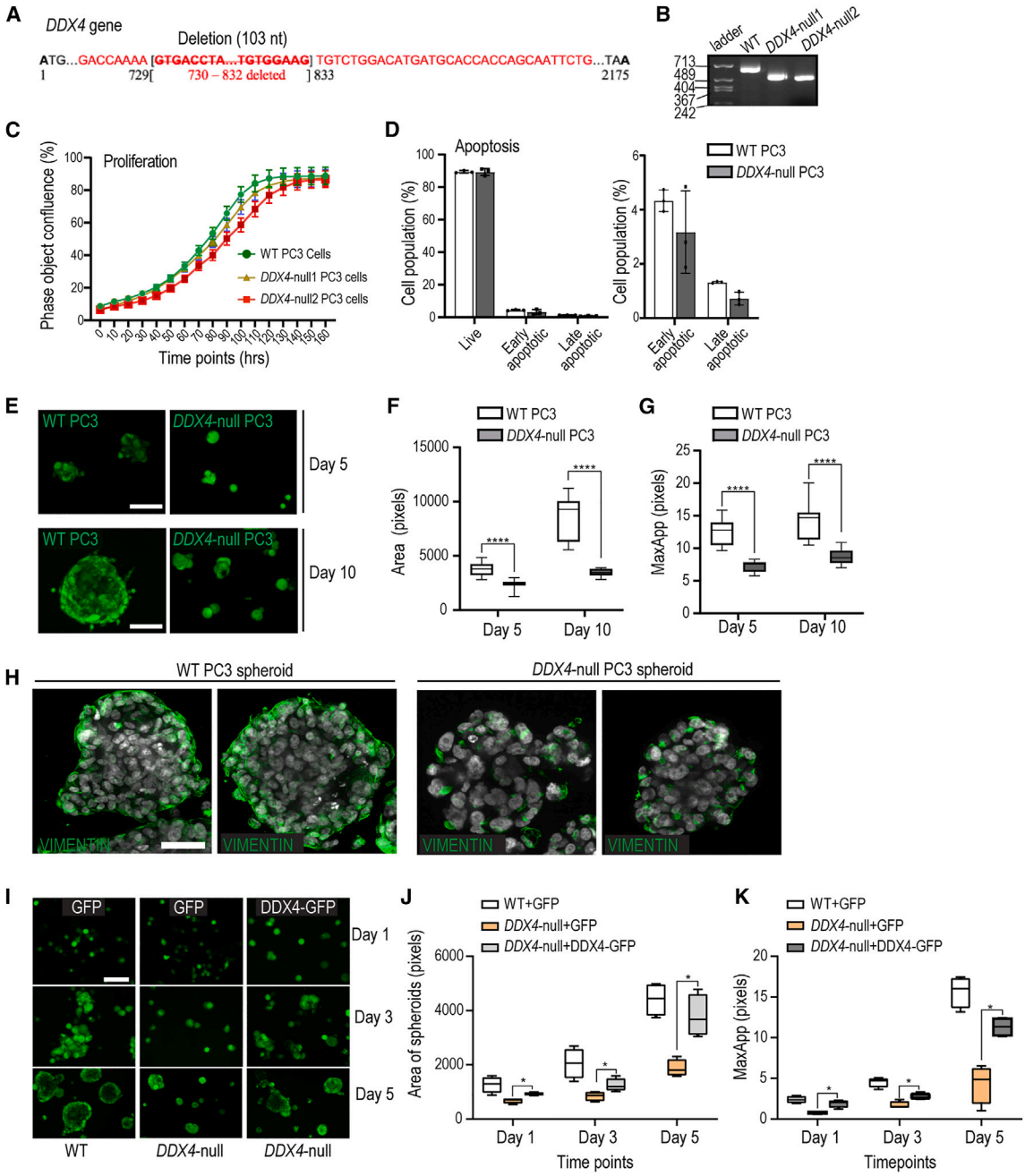

Figure 3. *DDX4* deletion compromises PC3 spheroid formation

(A) The sequence of *DDX*4 gene after CRISPR-Cas9 in PC3 cells to visualize the deleted 103 nt.

(B) Agarose gel of genomic PCR of WT and 2 *DDX4*-null PC3 cell clones (null1 and null2).

(C) Proliferation curve of *DDX4*-null and WT PC3 cells.

(D) Bar charts show the percentage of live cells, early apoptotic cells, and late apoptotic cells in WT and *DDX4*-null PC3 cells (3 replicates each). The chart at right shows only the early and late apoptotic cells.

(E) Calcein AM-stained (green) WT and *DDX4*-null PC3 spheroids at days 5 and 10. Scale bar: 20 μm.

(F) Area of spheroids formed by *DDX4*-null vs. WT PC3 spheroids (day 5: $p = 0.000043$, day 10: $p = 0.000011$, Mann-Whitney *U* test, 2-tailed).

(G) Invasive processes (MaxApp in AMIDA) of *DDX4*-null vs. WT PC3 spheroids (day 5: $p = 0.000011$, day 10: $p = 0.000022$, Mann-Whitney *U* test, 2-tailed).

(H) Immunofluorescence on WT and *DDX4*-null (number of replicates is 10 for each) PC3 spheroids with vimentin antibody (green). Nuclei were stained with DAPI (gray). Scale bar: 20 μm.

(I) Calcein AM-stained (green) spheroids derived from WT and *DDX4*-null PC3 cells overexpressing either GFP or DDX4-GFP. Scale bar: 20 μm.

(legend continued on next page)

differences in body weight were observed between mice carrying WT or *DDX4*-null tumors (Figure S2C). Immunofluorescence staining with an anti-DDX4 antibody validated the absence of DDX4 granules in *DDX4*-null-derived tumors (Figure 4C). In line with the observation in spheroids, the expression of vimentin was significantly diminished in *DDX4*-null tumors both by immunofluorescence and western blotting (Figures 4D and 4E). We also generated subcutaneous xenografts using WT and *DDX4*-null UT-SCC-14 cells and validated the reduced size of *DDX4*-null tumors (Figures S2D–S2G).

To test the effects of *DDX4* deletion on the metastatic potential of PC3 cells, we performed orthotopic inoculation of *DDX4*-null PC3 cells ($n = 10$) and WT PC3 cells ($n = 10$) into the prostate. After 8 weeks, the experiment was terminated, and the mice were scored for orthotopic tumors and primary tumor-derived metastases. We were able to retrieve 4 orthotopic primary tumors formed by WT PC3 cells and 2 primary tumors formed by *DDX4*-null PC3 cells. In agreement with subcutaneous tumor data, the growth of orthotopic *DDX4*-null tumors was delayed, and the tumors were smaller than WT tumors (Figure S2H). We also monitored the lymph nodes for potential metastases and found prominent metastases in mice inoculated with WT PC3 cells. Although some metastases were also observed in mice bearing *DDX4*-null PC3 xenograft tumors, the secondary tumors were significantly smaller than those derived from WT PC3 primary tumors (Figure S2H). These results demonstrate that the deletion of *DDX4* hinders PC3 tumor development and invasion potential *in vivo*.

Deletion of *DDX4* affects the expression of genes that support invasive properties

To understand the role of DDX4 in the regulation of cancer-promoting properties of PC3 cells, we carried out RNA-sequencing (RNA-seq) of the *DDX4*-null and WT PC3 cells cultured in monolayers and xenograft tumors. There were pronounced transcriptomic changes in *DDX4*-null vs. WT PC3 cells cultured under 2D conditions (Figures 5A and S3A; Table S1A). More than 3,500 genes were dysregulated in *DDX4*-null PC3 cells, 2,196 genes of which were upregulated (log2fold change [FC] ≥ 1, adjusted p value ≤ 0.05) and 1,328 genes were downregulated (log2FC ≤ -1, adjusted p value ≤ 0.05). Despite the fact that the xenograft tumor samples are quite heterogeneous in terms of cellular composition, we were still able to identify 88 upregulated and 54 downregulated genes in PC3 *DDX4*-null xenograft tumors compared to controls (Figure 5A; Table S1B). Importantly, 61% (54/88) of the genes upregulated in *DDX4*-null xenograft tumors were also upregulated in *DDX4*-null cells, demonstrating that DDX4 contributes to similar transcriptomic changes both in cultured cancer cells and tumors *in vivo* (Figure 5B). The Gene Ontology (GO) term analysis showed that many biological processes relevant to cancer development, such as cell-cell adhesion, cell junctions, and cell migration, were enriched among genes misregulated in both *DDX4*-null cells and *DDX4*-null tumors (Figures S3B–S3E), providing mechanistic support for the findings from 3D culture and xenografting experiments.

Given the delay in the growth of *DDX4*-null spheroids and tumors and their less invasive nature, we decided to focus on the known tumor suppressor genes, as well as genes that have been shown to promote tumor formation or epithelial-mesenchymal transition (EMT). We first analyzed the expression of previously characterized tumor suppressor genes (https://bioinfo.uth.edu/TSGene/) in *DDX4*-null tumors using the RNA-seq data and showed that 15 of them were among the differentially expressed genes (log2FC ≥ 1, adjusted p value ≤ 0.05). Interestingly, the majority (12) of them (*OPCML*: opioid binding protein/cell adhesion molecule-like, *NDN*: necdin, MAGE family member, *PPP1R1B*: protein phosphatase 1 regulatory inhibitor subunit 1B, *DCC*: DCC netrin 1 receptor, *CTDSPL*: CTD small phosphatase-like, *CAMK2N1*: calcium/calmodulin-dependent protein kinase II inhibitor 1, *DIRAS1*: DIRAS family GTPase 1, *PROX1*: prospero homeobox 1, *GJB2*: gap junction protein beta 2, *LOX*: lysyl oxidase, *GJA1*: gap junction protein alpha 1, and *CEACAM1*: CEA cell adhesion molecule 1) were more highly expressed in *DDX4*-null PC3 tumors (Figures 5C and 5D). Seven of these genes were also upregulated in *DDX4*-null cells grown in 2D culture conditions (*CTDSPL*, *CAMK2N1*, *PPP1R1B*, *PROX1*, *LOX*, *DIRAS1*, and *GJB2*) (Table S1). These results indicate that DDX4 is involved in the regulation of these tumor suppressor genes, supporting the tumor growth-promoting function of DDX4.

We also took a closer look at selected genes with reported functions in tumor formation, growth, and metastasis. C-type lectin-like receptor 2 (*CLEC2B*), which has been shown to inhibit gastric cancer metastasis,[3] was strongly upregulated in *DDX4*-null PC3 tumors (Figure 5D). ADAM metallopeptidase domain 12 (*ADAM12*), which, in contrast, promotes cancer metastasis in gastric cancer,[26] was downregulated in *DDX4*-null PC3 tumors (Figure 5D). The Cadherin family members cadherin 6 (*CDH6*) and cadherin 7 (*CDH7*), with known roles in promoting EMT and metastasis,[27,28] were also downregulated in *DDX4*-null tumors (Figure 5D) and in *DDX4*-null cell lines (Table S1). The misregulated mRNA levels of *ADAM12*, *CDH6*, and *CDH7*, together with other relevant genes (*CEACAM*, *SFRP1*, *CLEC2B*) were validated by qRT-PCR of *DDX4*-null vs. WT PC3 tumors (Figure 5E). Furthermore, many genes upregulated in subcutaneous *DDX4*-null PC3 tumors were also shown to be upregulated in orthotopic *DDX4*-null prostate tumors (Figure S4).

To study whether the downregulation of *CDH6* mRNA results in the reduction of CDH6 protein expression, we performed western blotting and revealed a 9-fold lower expression of CDH6 protein in *DDX4*-null tumors compared to WT tumors (Figure 5F). The protein level of another Cadherin family

(J) Quantification of the area of spheroids formed by GFP or DDX4-GFP overexpressing WT and *DDX4*-null PC3 cells, $n = 4$ for each condition (day 1: $p = 0.0286$, day 3: $p = 0.0286$, day 5: $p = 0.0286$, Mann-Whitney U test, 2-tailed).
(K) Invasive processes (MaxApp in AMIDA) of spheroids formed by GFP or DDX4-GFP overexpressing WT and *DDX4*-null PC3 cells (day 1: $p = 0.0286$, day 3: $p = 0.0286$, day 5: $p = 0.0286$, Mann-Whitney U test, 2-tailed).
Data are represented as mean ± SEM.
See also Figures S1 and S2.

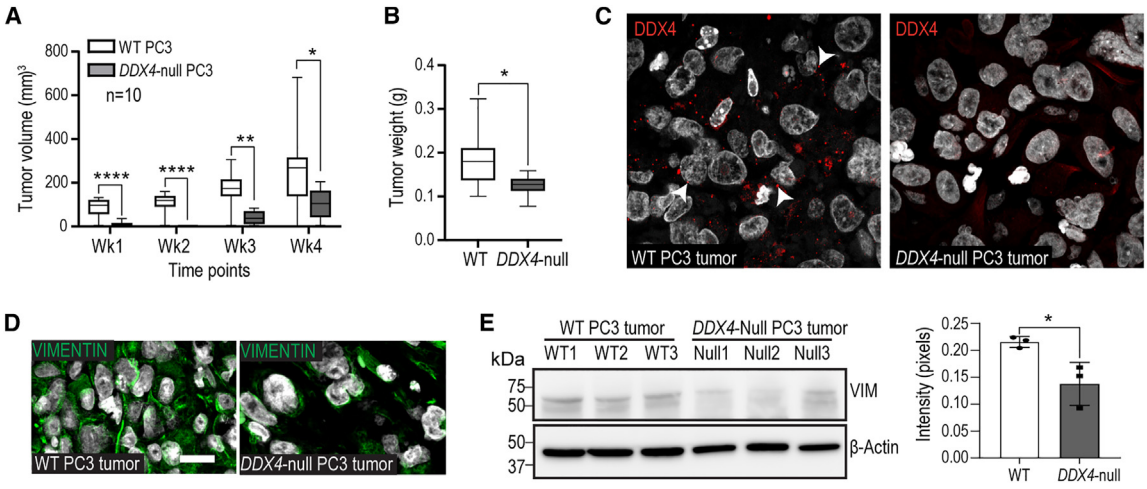

Figure 4. *DDX4* deletion compromises PC3 tumor formation and growth

(A) The volume of subcutaneous *DDX4*-null vs. WT PC3 xenograft tumors; 10 biological replicates each. The tumor progression was followed weekly for 4 weeks (Wk1: $p = 0.000411$, Wk2: $p = 0.000119$, Wk3: $p = 0.00105$, Wk4: $p = 0.006798$, Mann-Whitney *U* test, 2-tailed).

(B) The weights of dissected *DDX4*-null vs. WT PC3 tumors ($p = 0.0232$, Mann-Whitney *U* test, 2-tailed).

(C) Immunofluorescence with an anti-DDX4 antibody (red) validated the absence of DDX4 in *DDX4*-null PC3 tumor cells. Nuclei were stained with DAPI (gray). Scale bar: 20 μm.

(D) Immunofluorescence on *DDX4*-null and WT PC3 tumors with an anti-vimentin antibody (green). Scale bar: 10 μm.

(E) Western blotting of 3 biological replicates of WT and *DDX4*-null PC3 tumors with an anti-vimentin antibody. β-Actin was used as the loading control. The graph shows the quantification of vimentin signal (normalized to β-actin) ($p = 0.0309$, Mann-Whitney *U* test, 2-tailed).

Data are represented as mean ± SEM.

See also Figures S1 and S2.

member, cadherin 2 (*CDH2*), was not affected, which is in line with the unaffected mRNA expression in *DDX4*-null tumors (Table S1). Interestingly, although the mRNA expression of cadherin 1 (*CDH1*) was not affected (Table S1), the western blot analysis revealed a 3-fold higher expression of CDH1 (E-cadherin) protein in *DDX4*-null tumors. This supports the cancer-promoting function of DDX4, as CDH1 has been shown to have an opposite function to CDH6 and CDH7, and the loss of CDH1 expression in association with EMT occurs frequently during tumor metastasis.[29]

DDX4 forms complexes with mRNA regulatory proteins in cancer cells

To understand the mechanisms of DDX4 function in cancer, we immunoprecipitated (IP) DDX4 from PC3 subcutaneous xenograft tumors (Figure 6A) and identified DDX4-interacting proteins by mass spectrometry. We found 214 proteins that were present in both replicate DDX4-IP samples, but absent or at a very low level in the immunoglobulin (IgG) control sample (Table S2A). GO term analysis of the identified DDX4-interacting proteins emphasized the function of DDX4 in posttranscriptional mRNA regulation, since the most enriched biological processes included "translation," "regulation of RNA splicing," "regulation of mRNA processing," "RNA transport," and "RNA localization" (Figure 6B; Table S2B).

Among the most enriched cellular component GO term was "ribonucleoprotein granule," which substantiates the known role of DDX4 in germ granules.[15] Interestingly, 17 out of 88 previously identified components of the CB[13] were also found to form complexes with DDX4 in cancer-associated granules of PC3 xenografts (Figure 6C), indicating that the germ cell function of DDX4 is conserved in cancer cells, and the DDX4 granules resemble germ granules. In addition to known germ granule proteins, DDX4 complexes from PC3 xenografts included proteins involved in stress granule assembly and function in somatic cells (PRRC2C: proline rich coiled-coil 2C, PABPC1: poly(A) binding protein cytoplasmic 1, NUFIP2: nuclear FMR1 interacting protein 1, DDX1: DEAD-box helicase 1, DDX3X: DEAD-box helicase 3 X-linked, FMR1: fragile X messenger RNP 1, EIF3B: eukaryotic translation initiation factor 3 subunit B, PABPC4: poly(A) binding protein cytoplasmic 4, G3BP1: G3BP stress granule assembly factor 1, ATXN2L: ataxin 2-like, CAPRIN1: cell-cycle-associated protein 1, G3BP2: G3BP stress granule assembly factor 2, EIF4G1: eukaryotic translation initiation factor 4 gamma 1, YBX1: Y-box binding protein 1, IGF2BP2: insulin-like growth factor 2 mRNA-binding protein 2, EIF2S1: eukaryotic translation initiation factor 2 subunit alpha, ROCK1: Rho-associated coiled-coil containing protein kinase 1, GIGYF2: GRB10 interacting GYF protein 2, LARP1: La RNP 1, translational regulator, STAU1: staufen double-stranded RNA-binding protein 1). These data indicate that cancer cells could benefit from DDX4 function to form RNP granules for transcriptome regulation.

Surprisingly, no PIWI proteins were found among DDX4-interacting proteins despite their cooperation in the germ line.[19,30] We further addressed the possible role of DDX4 in the piRNA pathway by small RNA-seq of CTRL and *DDX4*-null PC3 cells and tumors. We showed that both PC3 cells and tumors have reads mapping to the piRNA clusters.[31,32] However, the

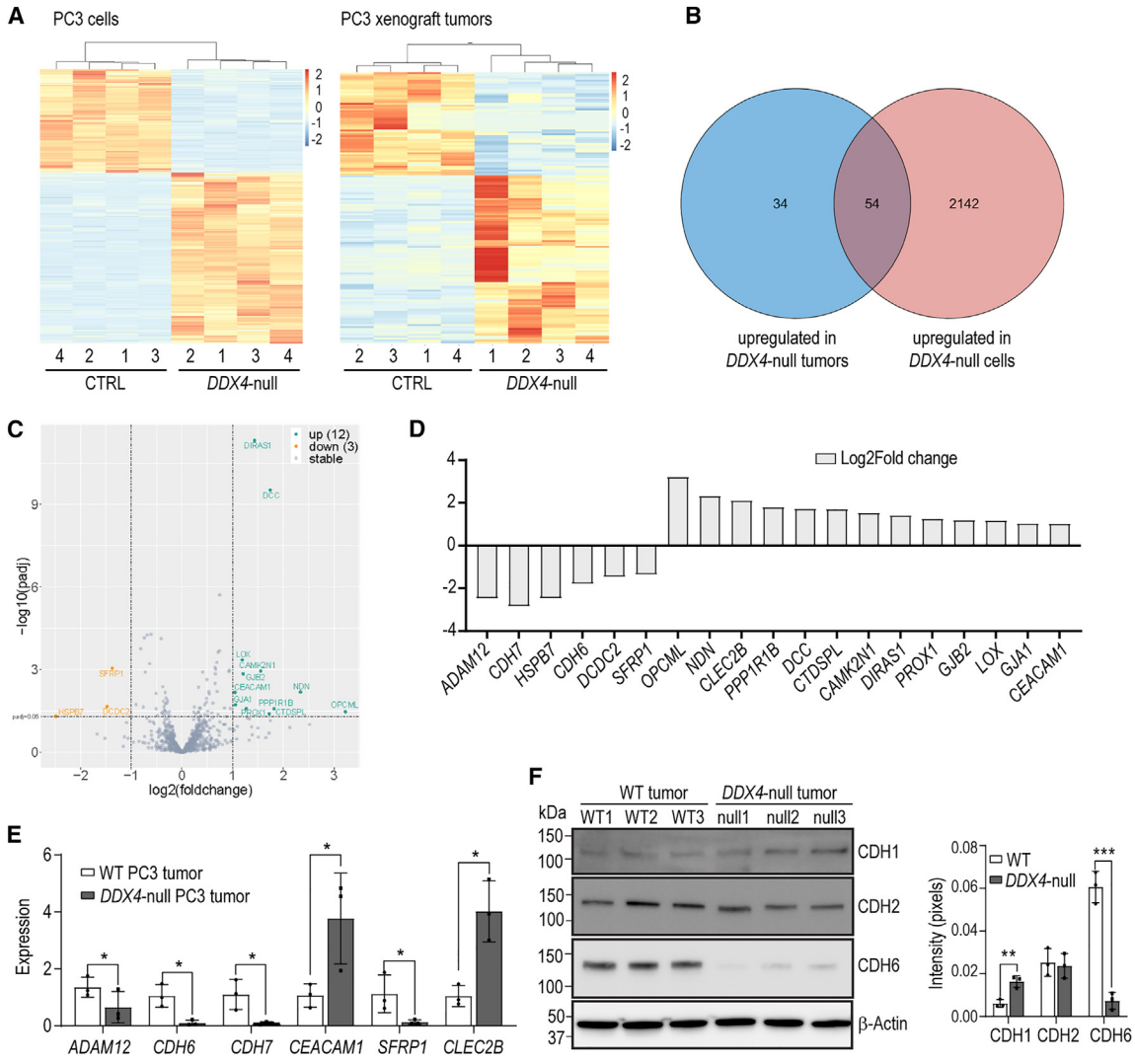

Figure 5. Transcriptome is misregulated in *DDX4*-null PC3 cells and *DDX4*-null PC3 xenograft tumors

(A) Hierarchical heatmaps show differentially expressed (|log2FC| ≥ 1, adjusted *p* value ≤0.05) genes in *DDX4*-null vs. WT PC3 cells (left) and xenograft tumors (right).

(B) Venn diagram shows the overlap between the genes upregulated in *DDX4*-null vs. WT PC3 xenograft tumors and cells.

(C) Volcano plot shows the differential expression of tumor suppressor genes in *DDX4*-null vs. WT PC3 tumors, with significantly upregulated (green) and downregulated (orange) genes labeled.

(D) Bar chart shows the log2FC (*DDX4*-null vs. WT tumors) of individually selected genes.

(E) Bar chart shows the validation of the selected differentially expressed genes in *DDX4*-null vs. WT PC3 tumors (number of biological replicates is 3) by qRT-PCR (*ADAM12*: $p = 0.0112$, *CDH6*: $p = 0.0161$, *CDH7*: $p = 0.0298$, *CEACAM1*: $p = 0.0468$, *SFRP1*: $p = 0.0293$, and *CLEC2B*: $p = 0.0105$, Mann-Whitney *U* test, 2-tailed).

(F) Western blotting image of CDH6, CDH1, and CDH2 protein expression in *DDX4*-null and WT PC3 tumors (3 biological replicates each). β-Actin was used as the loading control. Bar chart shows the quantification of the CDH1, CDH2, and CDH6 protein levels normalized by β-actin signal. CDH1: $p = 0.0055$, CDH6: $p = 0.0004$ (Mann-Whitney *U* test, 2-tailed, 3 biological replicates each).

Data are represented as mean ± SEM.

See also Figures S3 and S4 and Table S1.

abundance of cluster-derived piRNA reads was relatively low compared to the abundance of miRNA reads (Figure S5A). The bias toward having uridine (U) at their 5′ end, typical for the germline piRNAs,[33] was also absent (Figure S5B). Furthermore, their size distribution was different from the germline piRNAs, peaking at 23 nt instead of 29–31 nt, and the size distribution was not affected in *DDX4*-null cells or tumors (Figure S5A). These findings suggest that the cancerous function of DDX4 is not connected to the piRNA pathway.

Deletion of *DDX4* affects the splicing landscape of cancer cells

The high enrichment of proteins involved in the regulation of splicing among DDX4-interacting proteins (Figure 6B; Table S2)

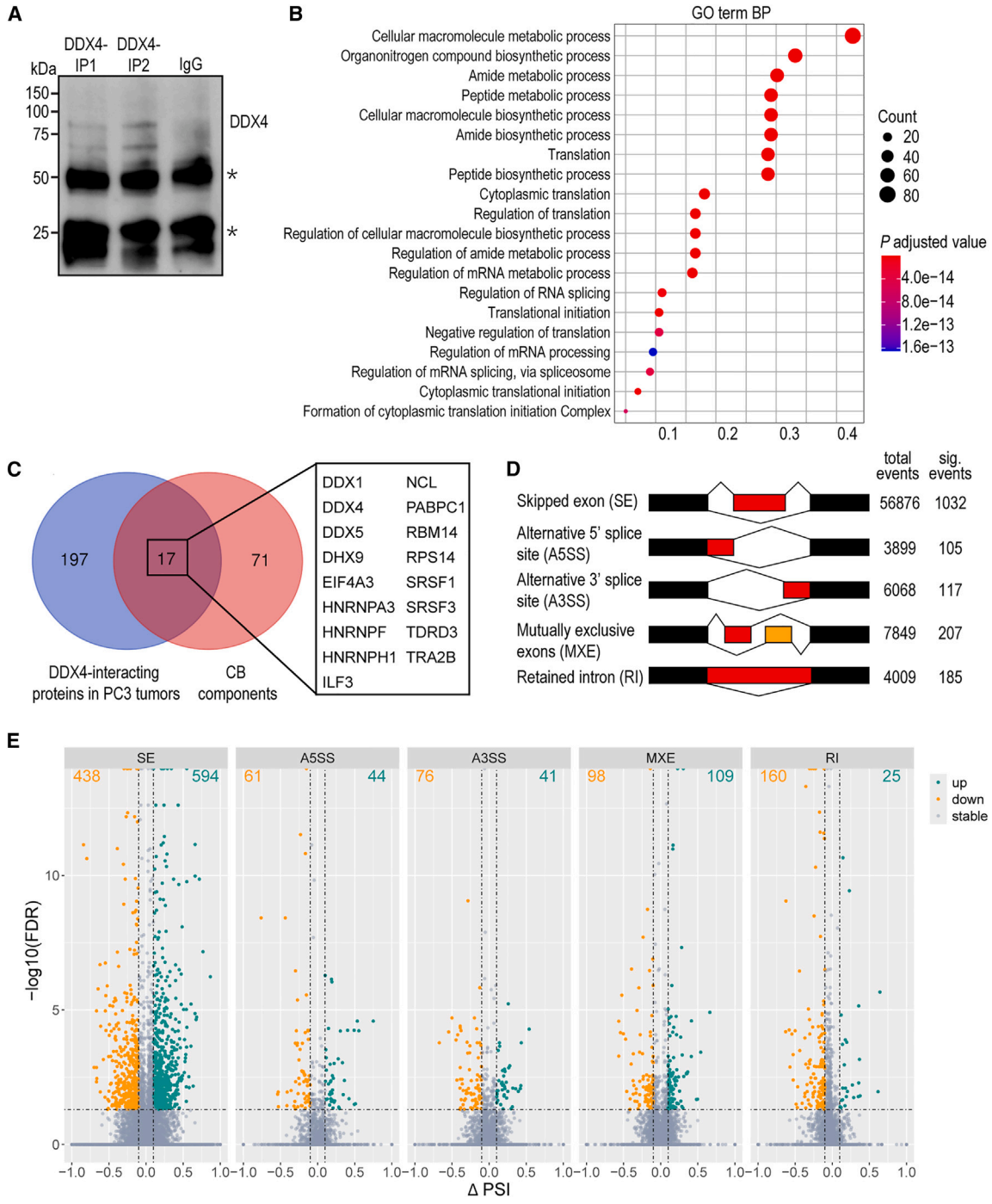

Figure 6. *DDX4* deletion affects the splicing landscape of cancer cells

(A) IP of PC3 tumors (2 biological replicates) with an anti-DDX4 antibody, followed by western blotting with the same antibody. IgG IP was used as the negative control. IgG light and heavy chains are indicated with asterisks.

(B) GO term enrichment analysis of the proteins interacting with DDX4 in PC3 xenograft tumors. Bubble plot visualizes the most enriched biological processes selected based on the adjusted *p* values. Gene ratio: The number of proteins that are associated with the GO term divided by the total number of proteins. Count: represents the number of proteins annotated to the GO term; the size of a bubble dot reflects the number of proteins.

(C) Venn diagram illustrating 17 shared components (listed in the rectangular box) between the CB and the DDX4-interacting proteins.

(legend continued on next page)

prompted us to investigate the splicing landscape in *DDX4*-null vs. WT PC3 cells. We analyzed 5 different splicing events: skipped exon (SE), alternative 5′ splice site (A5SS), alternative 3′ splice site (A3SS), mutually exclusive exons (MXE), and retained intron (RI) (Figure 6D). The SE was the most frequent alternative splicing type in PC3 cells, with 56,876 events identified, followed by MXE (7,849 events), A3SS (6,068 events), RI (4,009 events), and A5SS (3,899 events) (Figure 6D; Table S3). The comparison of *DDX4*-null vs. WT PC3 identified 1,646 (813 increased and 833 reduced) significantly different (false discovery rate [FDR] $\leq$0.05) alternative splicing events (originating from 1,207 genes) with more than 10% ΔPSI (percent spliced-in index) between the null and WT cells (Table S3). Only 67 of the differentially spliced genes were upregulated and 92 were downregulated in *DDX4*-null vs. WT PC3 cells ($|\log2FC| \geq 1$, adjusted p value $\leq$0.05; Figure S5C), indicating that the changes in splicing events did not affect the bulk expression of the majority of these genes. The most frequent differential alternative splicing event was SE (1,032 events), followed by MXE (207 events), RI (185 events), A3SS (117 events), and A5SS (105 events) (Figure 6D). Interestingly, while SE, MXE, A3SS, and A5SS events were quite equally either increased or decreased, the majority of the RI events were decreased (25 increased, 160 decreased) in *DDX4*-null vs. WT PC3 cells (Figure 6E). GO enrichment analysis showed that differentially alternatively spliced genes were connected to many processes with important roles in cancer cell proliferation and tumor formation and growth, including microtubule anchoring and spindle assembly, cell adhesion, and transcription and epigenetic regulation-related processes (Figure S5D). Furthermore, 6.5% (78/1,207) of genes with differential alternative splicing events overlapped with the known tumor suppressor genes (https://bioinfo.uth.edu/TSGene/), and 26% (309/1,207) overlapped with genes associated with EMT (www.emtome.org), indicating that these altered splicing events have the potential to affect cancer cell properties.

We also analyzed the differential alternative splicing events in *DDX4*-null vs. WT tumors. Despite the tumor heterogeneity, which interferes considerably with the analysis, we were able to identify a total of 446 significantly changed splicing events in 395 genes, and the splicing of 104 genes was affected in both *DDX4*-null cells and tumors (Table S4). Together, these results show that DDX4 contributes to the regulation of the alternative splicing landscape in PC3 cancer cells, and suggest that DDX4 promotes intron retention in cancer cell transcripts.

DDX4 has a prognostic significance in human cancers

Considering the cancer-promoting function of DDX4 in our experimental models, we decided to investigate the prognostic value of DDX4 granules in human cancers. We focused on HNSCC and PC, and scored the presence of DDX4-granules in 46 HNSCC and 164 PC patient samples. Cytoplasmic DDX4 granules were observed in 74% of both cancer types (HNSCC: 34/46, PC: 122/164) (Figures 7A and 7B). For DDX4$^+$ tumors, DDX4 granules were not found uniformly across the tumor samples, but intratumoral heterogeneity in DDX4 expression was observed (Figure S6A shows representative images of HNSCC tumors). The presence of DDX4 granules in the cytoplasm of cancer cells was not associated with the proliferation status of the cells, as DDX4 granules were found both in actively proliferating Ki-67$^+$ cells as well as in Ki-67$^-$ cells in HNSCC tumors (Figure S6B). Interestingly, in HNSCC patients, DDX4 expression was associated with the size of the tumor, as well as with tumor recurrence and poor survival (5 years) (Figures 7A and S7A). We also correlated DDX4 expression to clinical parameters in PC patients (Figure S7B) and showed that the expression of DDX4 in cancer epithelial cells was associated with the higher Gleason pattern in the core when the 3-tiered primary DDX4 score was used (Figure S7C). In addition, in low-grade disease (Gleason grade group $\leq$2), there was a trend toward a worse progression-free survival in patients with DDX4$^+$ cancer compared to patients with DDX4$^-$ cancer (Figure 7B). These results support our experimental data that DDX4 expression is favorable for cancer progression, and they implicate DDX4 as a prognostic marker.

DISCUSSION

Germline-specific genes are clearly beneficial for cancer cells, as supported by the expression of a high number of germline genes in somatic malignancies,[3] as well as the reported roles of many cancer-germline antigens in cancer initiation, progression, and metastasis.[4,34] One of the cancer-germline antigens with functional benefit for cancer cells is the RNA helicase DDX4.[35–39] Cancer cells share a lot of similarities with germ cells, including drastic epigenomic alterations and leaky transcription of the genome.[40–42] In germ cells, the broad genome-wide transcription is accompanied by the emergence of prominent cytoplasmic germ granules.[11] Our results suggest that analogously cancer cells harness germline-specific protein DDX4 and its germ-granule-related functions to support transcriptome regulation and to promote cancerous properties and tumor growth.

In the germ line, germ granules are tightly coupled with the biogenesis and function of piRNAs, and DDX4 cooperates with piRNA-interacting PIWI proteins in the production of piRNAs.[19,30] Although PIWI proteins have also been implicated as cancer-germline antigens,[43] we did not identify any PIWI proteins or piRNA biogenesis factors as DDX4-interacting proteins, and we did not observe any changes in the abundance or size distribution of piRNAs. This suggests that the germline function of DDX4 in the piRNA pathway is not conserved in cancer cells. In fact, although other studies have shown that piRNAs can be identified in cancer cells,[43] their functional role in cancer remains debatable.[33,44,45]

Instead of PIWI proteins, DDX4 formed complexes with a wide range of different RNA-binding and RNA-processing proteins in PC3 xenograft tumors. This, together with the dysregulation of

(D) Schematic diagram of the 5 different alternative splicing events analyzed using the RNA-seq data from *DDX4*-null and WT PC3 cells. Total detected events as well as significant events (FDR $\leq$0.05) with more than 10% ΔPSI between the null and WT cells are indicated for each splicing event.
(E) Volcano plots show the differential alternative splicing events in *DDX4*-null vs. WT PC3 cells. The events with $|\Delta PSI| \geq 0.1$, FDR $\leq$0.05, are indicated with colored dots.
See also Figure S5 and Tables S2, S3, and S4.

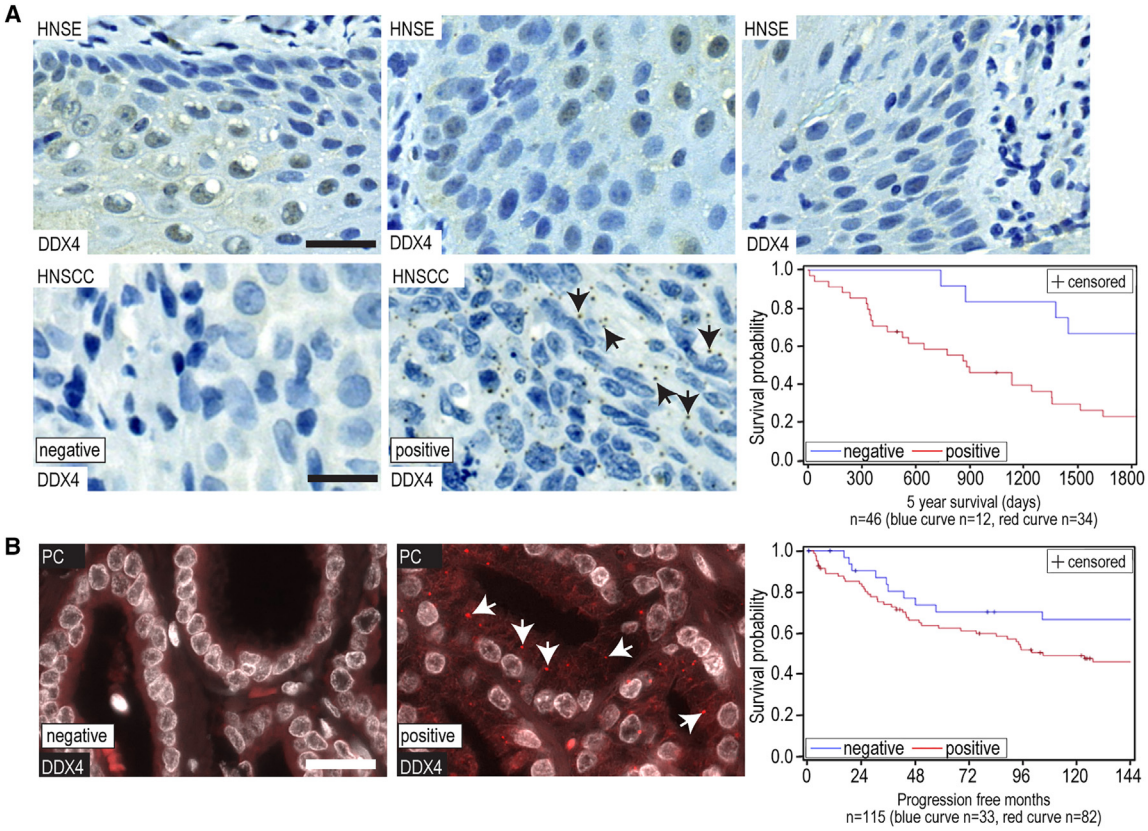

Figure 7. DDX4 has prognostic significance in human cancers

(A) Immunohistochemistry of normal head and neck squamous epithelium (HNSE, 3 representative examples) and HNSCC (bottom) with an anti-DDX4 antibody. The cells were counterstained with hematoxylin. HNSCC samples without granular DDX4 staining were scored as negative, while HNSCC samples with DDX4 granules (black arrows) were scored as positive. Scale bar: 20 μm. Survival curve shows 5-year survival (days) for DDX4$^-$ (n = 12/46) and DDX4$^+$ (n = 34/46) patients (p = 0.008, log rank test).

(B) Immunofluorescence on PC samples with an anti-DDX4 antibody. PC samples without granular DDX4 staining were scored as negative, while the PC samples with prominent DDX4 granules (white arrows) were scored as positive. Scale bar: 20 μm. Survival curve shows the progression-free survival (months) for DDX4$^-$ (n = 33/115) and DDX4$^+$ (n = 82/115) patients' samples with low-grade PC (Gleason grade group $\leq$2), (p = 0.080, log rank test).

See also Figures S6 and S7.

mRNA expression in the absence of DDX4, suggest that DDX4 functions in the cytoplasmic mRNA regulation in cancer cells. Many other DEAD-box RNA helicases have also been shown to function in a broad range of mRNA metabolic processes and in the assembly of RNP complexes and RNP granules in cancer cells to promote oncogenesis.[46–48] We found that DDX3X, DDX1, DDX5, and its paralog DDX17, all reported to be dysregulated in cancer and having cancer-associated functions,[47,49] formed complexes with DDX4 in PC3 xenograft tumors, indicating that the functions of these different helicases in mRNA regulation converge in cancer cells.

Cumulative evidence highlights the role of the assembly of RNP granules, such as stress granules and processing bodies, in supporting cellular cancerous properties.[50,51] Higher expression of RNP granule proteins in cancer has also been associated with poor prognosis.[10] The function of one of the DDX4-interacting RNA helicases, DDX3X, has previously been linked to RNP granules, and cancer-associated mutations of DDX3X have been shown to drive stress granule assembly, thus affecting the global translation.[52] Another stress granule protein-forming complex with DDX4 in PC3 xenograft tumors is G3BP1, which has been shown to promote tumor growth and metastasis in renal cell carcinoma.[53] This suggests that the germline-specific DDX4 can cooperate with stress granule proteins in RNA regulation to control cancer cells' transcriptome. Since stress-coping mechanisms are known to be important for tumor development and growth,[54,55] we speculate that DDX4 helps cancer cells to adapt to the stressful conditions caused by the tumor environment (e.g., in changes in cellular metabolisms and hypoxia).

The stress-granule-resembling function of DDX4 granules is further supported by our finding that puromycin treatment induced DDX4 granule formation in monolayer-cultured cells. Puromycin incorporation into growing polypeptide chains inhibits protein translation and leads to the release of truncated polypeptide chains and dissociation of polyribosomes.[56] This has been shown to cause an accumulation of free mRNA that promotes stress granule formation.[57] Similar to differentiating male germ cells,[41,42] cancer cells are known to undergo

pervasive transcription that produces high transcriptome diversity, including broad expression of the non-coding genome,[58] and we therefore speculate that the germ-granule-resembling DDX4 granules are formed to cope with the regulatory challenge generated by the high transcriptome diversity.[11]

Our analysis shows that many of the mRNAs that were affected in the absence of DDX4 have reported tumor formation-related functions, which is likely to explain the compromised spheroid formation and tumor growth. Considering the unaffected proliferation of monolayer-grown *DDX4*-null PC3 cells, it was somewhat unexpected that they had such massive dysregulation of gene expression. These results suggest that the affected genes are not needed for the proliferation of the monolayer-grown cells, but become critical only when the cells enter the tumor microenvironment. The dysregulation of gene expression in monolayer-grown cells is unlikely to be mediated by the granule-associated function of DDX4 due to the lack of granular staining in 2D conditions. Therefore, it appears that DDX4 can also regulate gene expression without forming prominent granules, and the granule-associated function of DDX4 is linked to the cellular stress response and formation of the tumor microenvironment.

The presence of a wide range of different splicing regulators in complex with DDX4, and the affected splicing landscape upon *DDX4* deletion, suggest a role for DDX4 in the regulation of the alternatively spliced transcripts in cancer cells. Altered splicing is known to contribute to cancer progression and metastasis, and alternative splicing events are considered to be potential targets for cancer treatments.[59–61] Interestingly, while *DDX4* deletion induced an imbalance in many different splicing events, intron retention was the only event showing bias toward being downregulated in the absence of DDX4. Widespread intron retention is common across cancers, even in the absence of mutations directly affecting the RNA splicing machinery, causing the accumulation of intron-containing transcripts and increasing transcriptome diversity, thereby offering grounds for gaining new malignant properties.[62,63] Intron retention is also active in differentiating male germ cells and contributes to the temporal regulation of gene expression during the time when DDX4 and germ granules are prominently expressed.[64] The misbalance in alternative splicing events in *DDX4*-null cancer cells could originate, for example, from defective targeting of alternatively spliced transcripts to cytoplasmic RNP granules.

While our data clearly demonstrate that DDX4 is beneficial for tumor growth and invasiveness, the role of DDX4 in the proliferation of monolayer-grown cancer cells is not as clear, as different results have been reported depending on the cell line. Although we did not see any significant effects on proliferation of *DDX4*-null PC3 cells, other studies have reported decreased proliferation of small cell lung cancer cells and multiple myeloma cells after *DDX4* deletion.[38,39] The mechanistic explanation for these differences remains to be characterized, but it may involve different epigenetic status or the stress-coping potential of these cell lines.

To provide clinical relevance to our findings, we showed that the presence of cytoplasmic DDX4 granules is associated with worse survival in HNSCC and worse prognosis in PC. HNSCC is a cancer with only a 50% 5-year survival rate,[65] and the lack of prognostic biomarkers is a challenge in the treatment stratification of HNSCC. In contrast to HNSCC, PC is a cancer with a more favorable prognosis. Still, there is a challenge in finding those patients whose cancer will progress and who should be followed more closely or treated more intensively. Our results suggest that DDX4 associates with aggressive disease in diverse cancers and that the assessment of DDX4 expression could aid in cancer prognostication. Furthermore, our findings that DDX4 can promote oncogenic processes and tumor growth, combined with its potentially druggable ATP-dependent helicase activity,[48] highlight DDX4 as an auspicious drug target for personalized therapeutic approaches. Although the targeting of DDX4 can have adverse effects on male fertility, its germline-specific expression would spare the somatic tissues from potential side effects.

Limitations of the study

Our results show that DDX4 granules appear in various types of cancers, but the functional studies were limited to the PC and HNSCC cell lines. Therefore, more studies are required to prove the universal functional role of DDX4 in different types of cancer. Low expression of DDX4 hindered some functional studies because the detection of DDX4 by western blotting was not possible without its enrichment by IP. Furthermore, the heterogeneous expression of DDX4 in tumors challenged particularly the RNA-seq analysis, and single-cell-level analysis is required to understand the specific role of DDX4 in individual cancer cells. We were also not able to discover the reason for the unaffected proliferation and apoptosis in monolayer-cultured *DDX4*-null cells despite the dramatic dysregulation of gene expression. Sequencing of *DDX4*-null vs. WT spheroids would be important to understand the effects of 2D vs. 3D culture conditions on DDX4 function, and further studies are also required to reveal the role of granule assembly in DDX4 function.

STAR★METHODS

Detailed methods are provided in the online version of this paper and include the following:

- KEY RESOURCES TABLE
- RESOURCE AVAILABILITY
  - Lead contact
  - Materials availability
  - Data and code availability
- EXPERIMENTAL MODEL AND STUDY PARTICIPANT DETAILS
  - Animals
  - Human samples
- METHOD DETAILS
  - Xenograft tumors
  - Cell culture
  - Organotypic 3D culture
  - Generation of *DDX4*-null cell lines
  - PCR screening of *DDX4* mutations
  - 2D proliferation assay
  - Apoptosis assay
  - Quantitative phenotypic analysis of spheroids
  - Transient overexpression of DDX4
  - Primary antibodies
  - Immunofluorescence
  - Immunohistochemistry and scoring

SUPPLEMENTAL INFORMATION

Supplemental information can be found online at https://doi.org/10.1016/j.celrep.2024.114430.

ACKNOWLEDGMENTS

This work was supported by the Academy of Finland, the Turku doctoral program of molecular medicine, the Sigrid Jusélius Foundation, the Novo Nordisk Foundation, the Jane and Aatos Erkko Foundation, and the Jalmari and Rauha Ahokas Foundation. We want to acknowledge the Turku Center for Disease Modeling, particularly Heli Niittymäki, Heidi Liljenbäck, and Katri Hovirinta, for the expert assistance in xenografting experiments; the Central Animal Facility of the University of Turku for the mouse facilities; and the Turku Bioscience Center for mass spectrometry and cell imaging facilities. We are grateful to Dr. Marcin Chrusciel and Dr. Nafis Rahman for generously giving us tumor samples for the initial testing of antibodies. We also thank Niina Smolander and Elina Tuomikoski for technical assistance in the experiments.

AUTHOR CONTRIBUTIONS

O.O. and N.K. conceived and designed the study. O.O., A.-R.K., V.P., Sini Laasanen, E. Louramo, T.L., Samuli Laasanen, A.R.-M., P.V., and J.-A.M. designed and performed the laboratory experiments and analyzed the data. L.M. and M.B. analyzed the RNA-seq data. E. Löyttyniemi performed the statistical analyses of the human samples. C.S., J.W., S.V., T.V., and M.P. provided samples and other resources to the study. O.O., A.-R.K., J.-A.M., and N.K. interpreted the data and drafted the manuscript. All authors reviewed and edited the final version of the manuscript.

DECLARATION OF INTERESTS

The authors declare no competing interests.

Received: November 12, 2023
Revised: May 15, 2024
Accepted: June 18, 2024

REFERENCES

1. Berdasco, M., and Esteller, M. (2010). Aberrant epigenetic landscape in cancer: how cellular identity goes awry. Dev. Cell *19*, 698–711. https://doi.org/10.1016/j.devcel.2010.10.005.
2. Rousseaux, S., Debernardi, A., Jacquiau, B., Vitte, A.-L., Vesin, A., Nagy-Mignotte, H., Moro-Sibilot, D., Brichon, P.-Y., Lantuejoul, S., Hainaut, P., et al. (2013). Ectopic activation of germline and placental genes identifies aggressive metastasis-prone lung cancers. Sci. Transl. Med. *5*, 186ra66. https://doi.org/10.1126/scitranslmed.3005723.
3. Wang, C., Gu, Y., Zhang, K., Xie, K., Zhu, M., Dai, N., Jiang, Y., Guo, X., Liu, M., Dai, J., et al. (2016). Systematic identification of genes with a cancer-testis expression pattern in 19 cancer types. Nat. Commun. *7*, 10499. https://doi.org/10.1038/ncomms10499.
4. Gibbs, Z.A., and Whitehurst, A.W. (2018). Emerging Contributions of Cancer/Testis Antigens to Neoplastic Behaviors. Trends Cancer *4*, 701–712. https://doi.org/10.1016/j.trecan.2018.08.005.
5. Meng, X., Sun, X., Liu, Z., and He, Y. (2021). A novel era of cancer/testis antigen in cancer immunotherapy. Int. Immunopharmacol. *98*, 107889. https://doi.org/10.1016/j.intimp.2021.107889.
6. Dreyfuss, G., Kim, V.N., and Kataoka, N. (2002). Messenger-RNA-binding proteins and the messages they carry. Nat. Rev. Mol. Cell Biol. *3*, 195–205. https://doi.org/10.1038/nrm760.
7. Bertoldo, J.B., Müller, S., and Hüttelmaier, S. (2023). RNA-binding proteins in cancer drug discovery. Drug Discov. Today *28*, 103580. https://doi.org/10.1016/j.drudis.2023.103580.
8. Hanahan, D., and Weinberg, R.A. (2011). Hallmarks of cancer: the next generation. Cell *144*, 646–674. https://doi.org/10.1016/j.cell.2011.02.013.
9. An, H., de Meritens, C.R., and Shelkovnikova, T.A. (2021). Connecting the "dots": RNP granule network in health and disease. Biochim. Biophys. acta. Mol. cell Res. *1868*, 119058. https://doi.org/10.1016/j.bbamcr.2021.119058.
10. Lavalée, M., Curdy, N., Laurent, C., Fournié, J.-J., and Franchini, D.-M. (2021). Cancer cell adaptability: turning ribonucleoprotein granules into targets. Trends Cancer *7*, 902–915. https://doi.org/10.1016/j.trecan.2021.05.006.
11. Lehtiniemi, T., and Kotaja, N. (2018). Germ granule-mediated RNA regulation in male germ cells. Reproduction *155*, R77–R91. https://doi.org/10.1530/REP-17-0356.
12. Kotaja, N., and Sassone-Corsi, P. (2007). The chromatoid body: a germ-cell-specific RNA-processing centre. Nat. Rev. Mol. Cell Biol. *8*, 85–90. https://doi.org/10.1038/nrm2081.
13. Meikar, O., Vagin, V.V., Chalmel, F., Sõstar, K., Lardenois, A., Hammell, M., Jin, Y., Da Ros, M., Wasik, K.A., Toppari, J., et al. (2014). An atlas of chromatoid body components. RNA *20*, 483–495. https://doi.org/10.1261/rna.043729.113.
14. Lehtiniemi, T., Bourgery, M., Ma, L., Ahmedani, A., Mäkelä, M., Asteljoki, J., Olotu, O., Laasanen, S., Zhang, F.-P., Tan, K., et al. (2022). SMG6 localizes to the chromatoid body and shapes the male germ cell transcriptome to drive spermatogenesis. Nucleic Acids Res. *50*, 11470–11491. https://doi.org/10.1093/NAR/GKAC900.
15. Xu, C., Cao, Y., and Bao, J. (2021). Building RNA-protein germ granules: insights from the multifaceted functions of DEAD-box helicase Vasa/Ddx4 in germline development. Cell. Mol. Life Sci. *79*, 4. https://doi.org/10.1007/s00018-021-04069-1.
16. Onohara, Y., Fujiwara, T., Yasukochi, T., Himeno, M., and Yokota, S. (2010). Localization of mouse vasa homolog protein in chromatoid body and related nuage structures of mammalian spermatogenic cells during spermatogenesis. Histochem. Cell Biol. *133*, 627–639. https://doi.org/10.1007/s00418-010-0699-5.
17. Fujiwara, Y., Komiya, T., Kawabata, H., Sato, M., Fujimoto, H., Furusawa, M., and Noce, T. (1994). Isolation of a DEAD-family protein gene that encodes a murine homolog of Drosophila vasa and its specific expression in germ cell lineage. Proc. Natl. Acad. Sci. USA *91*, 12258–12262.
18. Tanaka, S.S., Toyooka, Y., Akasu, R., Katoh-Fukui, Y., Nakahara, Y., Suzuki, R., Yokoyama, M., and Noce, T. (2000). The mouse homolog of Drosophila Vasa is required for the development of male germ cells. Genes Dev. *14*, 841–853.
19. Wenda, J.M., Homolka, D., Yang, Z., Spinelli, P., Sachidanandam, R., Pandey, R.R., and Pillai, R.S. (2017). Distinct Roles of RNA Helicases MVH and TDRD9 in PIWI Slicing-Triggered Mammalian piRNA Biogenesis and Function. Dev. Cell *41*, 623–637.e9. https://doi.org/10.1016/J.DEVCEL.2017.05.021.
20. Gustafsson, H., Kale, A., Dasu, A., Lund, A., Edqvist, P.-H., and Roberg, K. (2017). EPR Oximetry of Cetuximab-Treated Head-and-Neck Tumours in a Mouse Model. Cell Biochem. Biophys. *75*, 299–309. https://doi.org/10.1007/s12013-017-0814-5.
21. Tai, S., Sun, Y., Squires, J.M., Zhang, H., Oh, W.K., Liang, C.-Z., and Huang, J. (2011). PC3 is a cell line characteristic of prostatic small cell carcinoma. Prostate *71*, 1668–1679. https://doi.org/10.1002/pros.21383.

22. Kaighn, M.E., Narayan, K.S., Ohnuki, Y., Lechner, J.F., and Jones, L.W. (1979). Establishment and characterization of a human prostatic carcinoma cell line (PC-3). Invest. Urol. *17*, 16–23.

23. Härmä, V., Schukov, H.-P., Happonen, A., Ahonen, I., Virtanen, J., Siitari, H., Åkerfelt, M., Lötjönen, J., and Nees, M. (2014). Quantification of dynamic morphological drug responses in 3D organotypic cell cultures by automated image analysis. PLoS One *9*, e96426. https://doi.org/10.1371/journal.pone.0096426.

24. Gebhard, C., Gabriel, C., and Walter, I. (2016). Morphological and Immunohistochemical Characterization of Canine Osteosarcoma Spheroid Cell Cultures. Anat. Histol. Embryol. *45*, 219–230. https://doi.org/10.1111/ahe.12190.

25. Usman, S., Waseem, N.H., Nguyen, T.K.N., Mohsin, S., Jamal, A., Teh, M.-T., and Waseem, A. (2021). Vimentin Is at the Heart of Epithelial Mesenchymal Transition (EMT) Mediated Metastasis. Cancers *13*, 4985. https://doi.org/10.3390/cancers13194985.

26. Zhu, H., Jiang, W., Zhu, H., Hu, J., Tang, B., Zhou, Z., He, X., Zhu, H., Jiang, W., Zhu, H., et al. (2022). Elevation of ADAM12 facilitates tumor progression by enhancing metastasis and immune infiltration in gastric cancer. Int. J. Oncol. *60*, 51. https://doi.org/10.3892/ijo.2022.5341.

27. Machado, R.A.C., Schneider, H., DeOcesano-Pereira, C., Lichtenstein, F., Andrade, F., Fujita, A., Trombetta-Lima, M., Weller, M., Bowman-Colin, C., and Sogayar, M.C. (2019). CHD7 promotes glioblastoma cell motility and invasiveness through transcriptional modulation of an invasion signature. Sci. Rep. *9*, 3952. https://doi.org/10.1038/s41598-019-39564-w.

28. Zhao, Z., Li, S., Li, S., Wang, J., Lin, H., and Fu, W. (2021). High expression of oncogene cadherin-6 correlates with tumor progression and a poor prognosis in gastric cancer. Cancer Cell Int. *21*, 493. https://doi.org/10.1186/s12935-021-02071-y.

29. Petrova, Y.I., Schecterson, L., and Gumbiner, B.M. (2016). Roles for E-cadherin cell surface regulation in cancer. Mol. Biol. Cell *27*, 3233–3244. https://doi.org/10.1091/mbc.E16-01-0058.

30. Kuramochi-Miyagawa, S., Watanabe, T., Gotoh, K., Takamatsu, K., Chuma, S., Kojima-Kita, K., Shiromoto, Y., Asada, N., Toyoda, A., Fujiyama, A., et al. (2010). MVH in piRNA processing and gene silencing of retrotransposons. Genes Dev. *24*, 887–892. https://doi.org/10.1101/gad.1902110.

31. Li, X.Z., Roy, C.K., Dong, X., Bolcun-Filas, E., Wang, J., Han, B.W., Xu, J., Moore, M.J., Schimenti, J.C., Weng, Z., and Zamore, P.D. (2013). An ancient transcription factor initiates the burst of piRNA production during early meiosis in mouse testes. Mol. Cell *50*, 67–81. https://doi.org/10.1016/j.molcel.2013.02.016.

32. Özata, D.M., Yu, T., Mou, H., Gainetdinov, I., Colpan, C., Cecchini, K., Kaymaz, Y., Wu, P.H., Fan, K., Kucukural, A., et al. (2020). Evolutionarily conserved pachytene piRNA loci are highly divergent among modern humans. Nat. Ecol. Evol. *4*, 156–168. https://doi.org/10.1038/S41559-019-1065-1.

33. Wang, X., Ramat, A., Simonelig, M., and Liu, M.F. (2023). Emerging roles and functional mechanisms of PIWI-interacting RNAs. Nat. Rev. Mol. Cell Biol. *24*, 123–141. https://doi.org/10.1038/S41580-022-00528-0.

34. Janic, A., Mendizabal, L., Llamazares, S., Rossell, D., and Gonzalez, C. (2010). Ectopic expression of germline genes drives malignant brain tumor growth in Drosophila. Science *330*, 1824–1827. https://doi.org/10.1126/science.1195481.

35. Kim, K.H., Kang, Y.-J., Jo, J.O., Ock, M.S., Moon, S.H., Suh, D.S., Yoon, M.S., Park, E.-S., Jeong, N., Eo, W.-K., et al. (2014). DDX4 (DEAD box polypeptide 4) colocalizes with cancer stem cell marker CD133 in ovarian cancers. Biochem. Biophys. Res. Commun. *447*, 315–322. https://doi.org/10.1016/j.bbrc.2014.03.144.

36. Chen, Y., Sun, Z., Xu, J., Wang, P., Tang, J., Shi, X., Liu, J., Ren, F., and Xu, L. (2018). Vitamin D and DDX4 regulate the proliferation and invasion of ovarian cancer cells. Oncol. Lett. *16*, 905–909. https://doi.org/10.3892/ol.2018.8718.

37. Lee, H.J., Venkatarame Gowda Saralamma, V., Kim, S.M., Ha, S.E., Vetrivel, P., Kim, E.H., Lee, S.J., Heo, J.D., Rampogu, S., Lee, K.W., and Kim, G.S. (2018). Comparative Proteomic Profiling of Tumor-Associated Proteins in Human Gastric Cancer Cells Treated with Pectolinarigenin. Nutrients *10*, 1596. https://doi.org/10.3390/nu10111596.

38. Noyes, C., Kitajima, S., Li, F., Suita, Y., Miriyala, S., Isaac, S., Ahsan, N., Knelson, E., Vajdi, A., Tani, T., et al. (2023). The germline factor DDX4 contributes to the chemoresistance of small cell lung cancer cells. Biol. *6*, 65. https://doi.org/10.1038/s42003-023-04444-7.

39. Schudrowitz, N., Takagi, S., Wessel, G.M., and Yajima, M. (2017). Germline factor DDX4 functions in blood-derived cancer cell phenotypes. Cancer Sci. *108*, 1612–1619. https://doi.org/10.1111/cas.13299.

40. Van Tongelen, A., Loriot, A., and De Smet, C. (2017). Oncogenic roles of DNA hypomethylation through the activation of cancer-germline genes. Cancer Lett. *396*, 130–137. https://doi.org/10.1016/j.canlet.2017.03.029.

41. Soumillon, M., Necsulea, A., Weier, M., Brawand, D., Zhang, X., Gu, H., Barthès, P., Kokkinaki, M., Nef, S., Gnirke, A., et al. (2013). Cellular source and mechanisms of high transcriptome complexity in the Mammalian testis. Cell Rep. *3*, 2179–2190. https://doi.org/10.1016/j.celrep.2013.05.031.

42. Xia, B., Yan, Y., Baron, M., Wagner, F., Barkley, D., Chiodin, M., Kim, S.Y., Keefe, D.L., Alukal, J.P., Boeke, J.D., and Yanai, I. (2020). Widespread Transcriptional Scanning in the Testis Modulates Gene Evolution Rates. Cell *180*, 248–262.e21. https://doi.org/10.1016/j.cell.2019.12.015.

43. Yao, J., Xie, M., Ma, X., Song, J., Wang, Y., and Xue, X. (2022). PIWI-interacting RNAs in cancer: Biogenesis, function, and clinical significance. Front. Oncol. *12*, 5077. https://doi.org/10.3389/FONC.2022.965684/BIBTEX.

44. Genzor, P., Cordts, S.C., Bokil, N.V., and Haase, A.D. (2019). Aberrant expression of select piRNA-pathway genes does not reactivate piRNA silencing in cancer cells. Proc. Natl. Acad. Sci. USA *116*, 11111–11112. https://doi.org/10.1073/PNAS.1904498116.

45. Shi, S., Yang, Z.Z., Liu, S., Yang, F., and Lin, H. (2020). PIWIL1 promotes gastric cancer via a piRNA-independent mechanism. Proc. Natl. Acad. Sci. USA *117*, 22390–22401. https://doi.org/10.1073/PNAS.2008724117.

46. Putnam, A.A., and Jankowsky, E. (2013). DEAD-box helicases as integrators of RNA, nucleotide and protein binding. Biochim. Biophys. Acta *1829*, 884–893. https://doi.org/10.1016/j.bbagrm.2013.02.002.

47. Bohnsack, K.E., Yi, S., Venus, S., Jankowsky, E., and Bohnsack, M.T. (2023). Cellular functions of eukaryotic RNA helicases and their links to human diseases. Nat. Rev. Mol. Cell Biol. *24*, 749–769. https://doi.org/10.1038/s41580-023-00628-5.

48. Naineni, S.K., Robert, F., Nagar, B., and Pelletier, J. (2023). Targeting DEAD-box RNA helicases: The emergence of molecular staples. Wiley Interdiscip. Rev. RNA *14*, e1738. https://doi.org/10.1002/WRNA.1738.

49. Secchi, M., Lodola, C., Garbelli, A., Bione, S., and Maga, G. (2022). DEAD-Box RNA Helicases DDX3X and DDX5 as Oncogenes or Oncosuppressors: A Network Perspective. Cancers *14*, 3820. https://doi.org/10.3390/CANCERS14153820.

50. Kechavarzi, B., and Janga, S.C. (2014). Dissecting the expression landscape of RNA-binding proteins in human cancers. Genome Biol. *15*, R14. https://doi.org/10.1186/gb-2014-15-1-r14.

51. Neelamraju, Y., Gonzalez-Perez, A., Bhat-Nakshatri, P., Nakshatri, H., and Janga, S.C. (2018). Mutational landscape of RNA-binding proteins in human cancers. RNA Biol. *15*, 115–129. https://doi.org/10.1080/15476286.2017.1391436.

52. Valentin-Vega, Y.A., Wang, Y.D., Parker, M., Patmore, D.M., Kanagaraj, A., Moore, J., Rusch, M., Finkelstein, D., Ellison, D.W., Gilbertson, R.J., et al. (2016). Cancer-associated DDX3X mutations drive stress granule assembly and impair global translation. Sci. Rep. *6*, 25996. https://doi.org/10.1038/SREP25996.

53. Wang, Y., Fu, D., Chen, Y., Su, J., Wang, Y., Li, X., Zhai, W., Niu, Y., Yue, D., and Geng, H. (2018). G3BP1 promotes tumor progression and

metastasis through IL-6/G3BP1/STAT3 signaling axis in renal cell carcinomas. Cell Death Dis. *9*, 501. https://doi.org/10.1038/s41419-018-0504-2.

54. Anastasiou, D. (2017). Tumour microenvironment factors shaping the cancer metabolism landscape. Br. J. Cancer *116*, 277–286. https://doi.org/10.1038/bjc.2016.412.
55. Seebacher, N.A., Richardson, D.R., and Jansson, P.J. (2015). Glucose modulation induces reactive oxygen species and increases P-glycoprotein-mediated multidrug resistance to chemotherapeutics. Br. J. Pharmacol. *172*, 2557–2572. https://doi.org/10.1111/bph.13079.
56. Aviner, R. (2020). The science of puromycin: From studies of ribosome function to applications in biotechnology. Comput. Struct. Biotechnol. J. *18*, 1074–1083. https://doi.org/10.1016/J.CSBJ.2020.04.014.
57. Bounedjah, O., Desforges, B., Wu, T.D., Pioche-Durieu, C., Marco, S., Hamon, L., Curmi, P.A., Guerquin-Kern, J.L., Piétrement, O., and Pastré, D. (2014). Free mRNA in excess upon polysome dissociation is a scaffold for protein multimerization to form stress granules. Nucleic Acids Res. *42*, 8678–8691. https://doi.org/10.1093/NAR/GKU582.
58. Adnane, S., Marino, A., and Leucci, E. (2022). LncRNAs in human cancers: signal from noise. Trends Cell Biol. *32*, 565–573. https://doi.org/10.1016/J.TCB.2022.01.006.
59. Zhang, Y., Qian, J., Gu, C., and Yang, Y. (2021). Alternative splicing and cancer: a systematic review. Signal Transduct. Target. Ther. *6*, 78. https://doi.org/10.1038/s41392-021-00486-7.
60. Bonnal, S.C., López-Oreja, I., and Valcárcel, J. (2020). Roles and mechanisms of alternative splicing in cancer — implications for care. Nat. Rev. Clin. Oncol. *17*, 457–474. https://doi.org/10.1038/s41571-020-0350-x.
61. Martinez-Montiel, N., Rosas-Murrieta, N.H., Anaya Ruiz, M., Monjaraz-Guzman, E., and Martinez-Contreras, R. (2018). Alternative Splicing as a Target for Cancer Treatment. Int. J. Mol. Sci. *19*, 545. https://doi.org/10.3390/ijms19020545.
62. Dvinge, H., and Bradley, R.K. (2015). Widespread intron retention diversifies most cancer transcriptomes. Genome Med. *7*, 45. https://doi.org/10.1186/s13073-015-0168-9.
63. Monteuuis, G., Schmitz, U., Petrova, V., Kearney, P.S., and Rasko, J.E.J. (2021). Holding on to Junk Bonds: Intron Retention in Cancer and Therapy. Cancer Res. *81*, 779–789. https://doi.org/10.1158/0008-5472.CAN-20-1943.
64. Naro, C., Jolly, A., Di Persio, S., Bielli, P., Setterblad, N., Alberdi, A.J., Vicini, E., Geremia, R., De la Grange, P., and Sette, C. (2017). An Orchestrated Intron Retention Program in Meiosis Controls Timely Usage of Transcripts during Germ Cell Differentiation. Dev. Cell *41*, 82–93.e4. https://doi.org/10.1016/j.devcel.2017.03.003.
65. Gatta, G., Botta, L., Sánchez, M.J., Anderson, L.A., Pierannunzio, D., and Licitra, L.; EUROCARE Working Group: (2015). Prognoses and improvement for head and neck cancers diagnosed in Europe in early 2000s: The EUROCARE-5 population-based study. Eur. J. Cancer *51*, 2130–2143. https://doi.org/10.1016/j.ejca.2015.07.043.
66. Schneider, C.A., Rasband, W.S., and Eliceiri, K.W. (2012). NIH Image to ImageJ: 25 years of image analysis. Nat. Methods *9*, 671–675. https://doi.org/10.1038/nmeth.2089.
67. Bolger, A.M., Lohse, M., and Usadel, B. (2014). Trimmomatic: a flexible trimmer for Illumina sequence data. Bioinformatics *30*, 2114–2120. https://doi.org/10.1093/bioinformatics/btu170.
68. Dobin, A., Davis, C.A., Schlesinger, F., Drenkow, J., Zaleski, C., Jha, S., Batut, P., Chaisson, M., and Gingeras, T.R. (2013). STAR: ultrafast universal RNA-seq aligner. Bioinformatics *29*, 15–21. https://doi.org/10.1093/bioinformatics/bts635.
69. Liao, Y., Smyth, G.K., and Shi, W. (2014). FeatureCounts: An efficient general purpose program for assigning sequence reads to genomic features. Bioinformatics *30*, 923–930. https://doi.org/10.1093/bioinformatics/btt656.
70. Love, M.I., Huber, W., and Anders, S. (2014). Moderated estimation of fold change and dispersion for RNA-seq data with DESeq2. Genome Biol. *15*, 550. https://doi.org/10.1186/s13059-014-0550-8.
71. Shen, S., Park, J.W., Lu, Z.X., Lin, L., Henry, M.D., Wu, Y.N., Zhou, Q., and Xing, Y. (2014). rMATS: Robust and flexible detection of differential alternative splicing from replicate RNA-Seq data. Proc. Natl. Acad. Sci. USA *111*, E5593–E5601. https://doi.org/10.1073/pnas.1419161111.
72. Shi, J., Ko, E.-A., Sanders, K.M., Chen, Q., and Zhou, T. (2018). SPORTS1.0: A Tool for Annotating and Profiling Non-coding RNAs Optimized for rRNA- and tRNA-derived Small RNAs. Dev. Reprod. Biol. *16*, 144–151. https://doi.org/10.1016/j.gpb.2018.04.004.
73. Kim, D., Paggi, J.M., Park, C., Bennett, C., and Salzberg, S.L. (2019). Graph-based genome alignment and genotyping with HISAT2 and HISAT-genotype. Nat. Biotechnol. *37*, 907–915. https://doi.org/10.1038/S41587-019-0201-4.
74. Euhus, D.M., Hudd, C., LaRegina, M.C., and Johnson, F.E. (1986). Tumor measurement in the nude mouse. J. Surg. Oncol. *31*, 229–234. https://doi.org/10.1002/jso.2930310402.
75. Tomayko, M.M., and Reynolds, C.P. (1989). Determination of subcutaneous tumor size in athymic (nude) mice. Cancer Chemother. Pharmacol. *24*, 148–154. https://doi.org/10.1007/bf00300234.
76. Tuomela, J.M., Valta, M.P., Väänänen, K., and Härkönen, P.L. (2008). Alendronate decreases orthotopic PC-3 prostate tumor growth and metastasis to prostate-draining lymph nodes in nude mice. BMC Cancer *8*, 81. https://doi.org/10.1186/1471-2407-8-81.
77. Ventelä, S., Sittig, E., Mannermaa, L., Mäkelä, J.A., Kulmala, J., Löyttyniemi, E., Strauss, L., Cárpen, O., Toppari, J., Grénman, R., and Westermarck, J. (2015). CIP2A is an Oct4 target gene involved in head and neck squamous cell cancer oncogenicity and radioresistance. Oncotarget *6*, 144–158. https://doi.org/10.18632/ONCOTARGET.2670.
78. Cong, L., and Zhang, F. (2015). Genome engineering using CRISPR-Cas9 system. Methods Mol. Biol. *1239*, 197–217. https://doi.org/10.1007/978-1-4939-1862-1_10.
79. Concordet, J.-P., and Haeussler, M. (2018). CRISPOR: intuitive guide selection for CRISPR/Cas9 genome editing experiments and screens. Nucleic Acids Res. *46*, W242–W245. https://doi.org/10.1093/nar/gky354.
80. Ran, F.A., Hsu, P.D., Wright, J., Agarwala, V., Scott, D.A., and Zhang, F. (2013). Genome engineering using the CRISPR-Cas9 system. Nat. Protoc. *8*, 2281–2308. https://doi.org/10.1038/nprot.2013.143.
81. Paramonov, V.M., Desai, D., Kettiger, H., Mamaeva, V., Rosenholm, J.M., Sahlgren, C., and Rivero-Müller, A. (2018). Targeting Somatostatin Receptors By Functionalized Mesoporous Silica Nanoparticles - Are We Striking Home? Nanotheranostics *2*, 320–346. https://doi.org/10.7150/ntno.23826.

STAR★METHODS

KEY RESOURCES TABLE

REAGENT or RESOURCE	SOURCE	IDENTIFIER
Antibodies		
Rabbit polyclonal anti-DDX4	Abcam	Cat# ab13840; RRID:AB_443012
Mouse anti- αTubulin	Neomarkers	Cat# MS-581-P1
Mouse monoclonal anti-Vimentin	GeneTex	Cat# GTX40346; RRID:AB_425224
Rabbit polyclonal anti-DDX4	Proteintech	Cat# 510421-1-AP; RRID:AB_2092998
Mouse monoclonal anti-CDH1	Cell Signaling Technology	Cat# 14472S; RRID: AB_2728770
Mouse monoclonal anti-CDH2	R&D Systems	Cat# MAB13881; RRID:AB_10973316
Rabbit polyclonal anti-CDH6	Cell Signaling Technology	Cat# 48111S; RRID:AB_2799334
Bacterial and virus strains		
10-beta Competent *E. coli* (High Efficiency)	New England Biolabs	C3019H
Biological samples		
Tissue microarray: Multiple organ tumor tissue array	Tissue Array	TP481a, AJCC7th version
Soft tissue tumor microarray	Tissue Array	T242b, AJCC 7th version
Head and Neck squamous cell carcinoma patient samples	Turku University Hospital	N/A
Prostate cancer patient samples	Tampere University Hospital	N/A
Chemicals, peptides, and recombinant proteins		
DMEM/F12	Sigma	Cat# D-18900
Fetal Bovine Serum	Biowest	Cat# S1810
Penicillin/Streptomycin	Gibco Life Technology	Cat# 15140-122
BD Matrigel GFR Basement membrane matrix, Phenol Red-free	BD Biosciences	Cat# 356237
Puromycin	ThermoFisher	Cat# A1113803
Carprofen	Pfizer SA, Louvain-La-Neuve, Belgium	N/A
Buprenorphine	Schering-Plough Nv, Brussels, Belgium	N/A
Midori Advanced	Nippon Genetics Europe	Cat# MG04
Xfect reagent	Clonetech Laboratories	Cat# 631317 & 631318
Critical commercial assays		
Annexin V-FITC fluorescence binding assay kit	Cell Signaling Technology	Cat #6592
Mouse Direct PCR Kit (For Genotyping)	Bimake	Cat #B40015
Deposited data		
RNA sequencing data	NCBI	GSE262574
Proteomic data	ProteomeXchange Consortium	PXD044856
Raw data from figures	Mendeley	https://doi.org/10.17632/hrrbdn58mn.1
Experimental models: Cell lines		
PC-3 cell line (human)	ATCC	CRL-1435
UT-SCC-14 cell line (human)	Cellosaurus	CVCL_7810
Experimental models: Organisms/strains		
Hsd:Athymic Nude-*Foxn1*^{nu}	Envigo France	N/A
Oligonucleotides		
Primer #1: tttttgtgatgctcgtcagg (forward)	IDT	N/A
Primer #2: gggcgtacttggcatatgat (reverse)	IDT	N/A

(*Continued on next page*)

Continued

REAGENT or RESOURCE	SOURCE	IDENTIFIER
Primer #3: gcacagccttacatcttgacc (forward)	IDT	N/A
Primer #4: cagaattgctggtggtgcat (reverse)	IDT	N/A
Primer #5: ttaaaggtaagcagtgggaagtt (forward)	IDT	N/A
Primer #6: tggggagtggggatgaaatcta (reverse)	IDT	N/A
ADAM12 primer: CGAGGGGTGAGC TTATGGAAC (forward)	IDT	N/A
ADAM12 primer: GCTTTCCCGTTGT AGTCGAATA (reverse)	IDT	N/A
ANKH primer: CATCACCAACATAGC CATCGAC (forward)	IDT	N/A
ANKH primer: GCCAGCATCTCGAC TGCAT (reverse)	IDT	N/A
CACNAH1 primer: ATGCTGGTAATC ATGCTCAACTG (forward)	IDT	N/A
CACNAH1 primer: AAAAGGCGAAAA TGAAGGCGT (reverse)	IDT	N/A
CDH6 primer: AGAACTTACCGCTAC TTCTTGC (forward)	IDT	N/A
CDH6 primer: TGCCCACATACTGAT AATCGGA (reverse)	IDT	N/A
CDH7 primer: TCAAATACATCTTGT CAGGCGAA (forward)	IDT	N/A
CDH7 primer: TCAAATACATCTTGT CAGGCGAA (reverse)	IDT	N/A
CEACAM1 primer: TGCTCTGATAGC AGTAGCCCT (forward)	IDT	N/A
CEACAM1 primer: TGCCGGTCTTCC CGAAATG (reverse)	IDT	N/A
CLEC2B primer: GTTCCACTCAACA TGCCGAC (forward)	IDT	N/A
CLEC2B primer: TGCCATCTTCAGT CCAATCCA (reverse)	IDT	N/A
CSPG4 primer: CTTTGACCCTGACT ATGTTGGC (forward)	IDT	N/A
CSPG4 primer: TGCAGGCGTCCAG AGTAGA (reverse)	IDT	N/A
HSD17B2 primer: TCTTCTCGGTGTC ATGCTTCC (forward)	IDT	N/A
HSD17B2 primer: CAAAACTCCGGC AAATACCGT (reverse)	IDT	N/A
IGSF9B primer: AGAGGAGCCCGAG TTTGTGA (forward)	IDT	N/A
IGSF9B primer: CACTCTACGACATA GGGTGGG (reverse)	IDT	N/A
MUC2 primer: GAGGGCAGAACCCG AAACC (forward)	IDT	N/A
MUC2 primer: GGCGAAGTTGTAGTC GCAGAG (reverse)	IDT	N/A
MGP primer: TCCGAGAACGCTCTA AGCCT (forward)	IDT	N/A
MGP primer: GCAAAGTCTGTAGTC ATCACAGG (reverse)	IDT	N/A

(*Continued on next page*)

Continued

REAGENT or RESOURCE	SOURCE	IDENTIFIER
RPL19 primer: AGGCACATGGGCA TAGGTAA (forward)	IDT	N/A
RPL19 primer: CCATGAGAATCCG CTTGTTT (reverse)	IDT	N/A
SFRP1 primer: ACGTGGGCTACAA GAAGATGG (forward)	IDT	N/A
SFRP1 primer: CAGCGACACGGG TAGATGG (reverse)	IDT	N/A
SMOC1 primer: AGGTCCTACGAG TCCATGTGT (forward)	IDT	N/A
SMOC1 primer: CACTGCACCTGG GTAAAGG (reverse)	IDT	N/A
DDX4 2xgRNA gene block (sequence (5′-3′)): cctttggaagacctCACCGGGGGTATGTAGGTC ACTTTGTTTTAGAGCTAGAAATAGCAAGTTA AAATAAGGCTAGTCCGTTATCAACTTGAAAA AGTGGCACCGAGTCGGTGCTTTTTTTCTAGA CCCAGCTTTCTTGTTGTACAAAAAAGCAGGC TTTAAAGGAACCAATTCAGTCGACTGGATCC GGTACCAAGGTCGGGCAGGAAGAGGGCCT ATTTCCCATGATTCCTTCATATTTGCATATAC GATACAAGGCTGTTAGAGAGATAATTAGAAT TAATTTGACTGTAAACACAAAGATATTAGTAC AAAATACGTGACGTAGAAAGTAATAATTTCTT GGGTAGTTTGCAGTTTTAAAATTATGTTTTAA AATGGACTATCATATGCTTACCGTAACTTGA AAGTATTTCGATTTCTTGGCTTTATATATCTT GTGGAAAGGACGAAACACCGACTATTCTTG TGGAAGTGTCGTTTgggtcttcgagctag	IDT	N/A
1st gRNA: GGGGGTATGTAGGTCACTTT tgg	IDT	N/A
2nd gRNA: ACTATTCTTGTGGAAGTGTC tgg	IDT	N/A
Recombinant DNA		
pSpCas9(BB)-2A-Puro (PX459) V2.0	Addgene	Cat # 62988: RRID:Addgene_62988
DDX4 (tGFP-tagged)	Origene	Cat# RG210628
Software and algorithms		
ImageJ 1.48	Schneider et al.[66]	N/A
AMIDA software	Härmä et al.[23]	N/A
Prism 9.0	GraphPad Software, Inc.	N/A
LAS4000	Fujifilm	N/A
Gel Imaging system	Led Nippon Genetics	Cat #GP-07
FastQC v0.11.9	Babraham Institute	http://www.bioinformatics.babraham.ac.uk/projects/fastqc/
Trimmomatic v0.39	Bolger et al.[67]	http://www.usadellab.org/cms/?page=trimmomatic
STAR v2.7.10a	Dobin et al.[68]	https://github.com/alexdobin/STAR
featureCounts v2.0.3	Liao et al.[69]	https://subread.sourceforge.net/
DESeq2 v1.40.2	Love et al.[70]	https://bioconductor.org/packages/devel/bioc/vignettes/DESeq2/inst/doc/DESeq2.html
rMATS v4.1.2	Shen et al.[71]	https://rnaseq-mats.sourceforge.io/
Cutadapt	https://doi.org/10.14806/ej.17.1.200.	https://cutadapt.readthedocs.io/en/stable/
SPORTS v1.1	Shi et al.[72]	https://github.com/junchaoshi/sports1.1
HISAT2	Kim et al.[73]	http://daehwankimlab.github.io/hisat2/

RESOURCE AVAILABILITY

Lead contact

Further information and requests for resources and reagents should be directed to and will be fulfilled by the lead contact, Noora Kotaja (nookot@utu.fi).

Materials availability

This study did not generate new unique reagents.

Data and code availability

- The RNA sequencing data generated in this study have been deposited in the National Center for Biotechnology Information's (NCBI) GEO database under accession number GSE262574. The mass spectrometry proteomics data have been deposited to the ProteomeXchange Consortium via the PRIDE partner repository with the dataset identifier PXD044856. Raw data from Figures were deposited on Mendeley (https://doi.org/10.17632/hrrbdn58mn.1). These data are publicly available as of the date of publication. Accession numbers are listed in the key resources table. All other data, and any additional information required to re-analyze the data reported in this paper are available from the lead contact upon request.
- Scripts and code utilized in this study are available from the lead contact upon request.
- Any additional information required to reanalyze the data reported in this work paper is available from the lead contact upon request.

EXPERIMENTAL MODEL AND STUDY PARTICIPANT DETAILS

Animals

All animal experiments were carried out according to the Finnish legislation and protocols approved by the ethical committee of animal experimentation at University of Turku Central Animal Laboratory, in agreement with good laboratory practice with project license number: 21485/2020, development and use of *in vivo* cancer models in research and drug development. 6–8 weeks old Hsd: Athymic Nude-*Foxn1*^{nu} male mice (Envigo, France) were used for the xenograft experiments. Mice were housed (10 mice per group to generate PC3 tumors, 15 per group to generate UT-SCC-14 tumors) in ventilated cages under controlled conditions of 12 h light and 12 h dark, humidity (55% ± 15%), and temperature of (21 ± 3°C). The mice were fed with Teklad 2920 soy-free, irradiated, with 20% protein (RM3; Special Diet Services, Witham, UK) and autoclaved or UV-treated water *ad libitum*. Mice were allowed to acclimatize 1–2 weeks before initiating the xenograft experiments.

Human samples

The collection and use of human material were approved by the Finnish national authority for medico-legal affairs and the regional ethics committee. For head and neck squamous cell carcinoma (HNSCC), a representative cohort of 46 patients diagnosed in Turku University Hospital in Finland was used. The median age of HNSCC patients at diagnosis was 65.5 years, and the mean/median follow-up times were 44/48 months, respectively. The most common site of the primary tumor was the oral cavity (48%, n = 22/46), followed by oropharyngeal tumors in 14 patients (30%, n = 14/46). Prostate cancer (PC) patients, n = 164 were treated by prostatectomy in Tampere University Hospital. The median age of the PC patients at diagnosis was 63 years, and the mean and median follow-up times were 54 and 38 months, respectively. The Gleason pattern was given by pathologists for every TMA core, being pattern 3 in 74% (n = 122/164) of the cases and 4 or 5 in 26% (n = 44/164) of the cases. The median PSA at the diagnosis was 10.8 μg/L. Formalin-fixed paraffin-embedded cancer tissue samples of the patients were collected from the pathology archives. A tissue microarray (TMA) for both patient cancer sample groups was created using 0.6 mm core from each paraffin block. Other human cancer samples used in the study were purchased as commercial TMAs: (1) Multiple organ tumor tissue array (TP481a, AJCC 7th version), core diameter 1.5 mm, containing normal tissue (breast, colon and lung), breast invasive carcinoma, colon adenocarcinoma, and lung adenocarcinoma samples, and (2) Soft tissue tumor microarray (T242b, AJCC 7th version), core diameter 1.5 mm, containing fibrosarcoma and leiomyosarcoma samples.

METHOD DETAILS

Xenograft tumors

To generate subcutaneous tumors, mice were anesthetized with isoflurane, and PC3 cells or UT-SCC-14 cells in DMEM/F12 were mixed with Corning matrigel (ratio 1:1) and inoculated subcutaneously (10^6 cells in 50 μL per right and left flanks). Tumor burden was assessed twice per week by measuring the length and width of tumors using digital calipers or an ultrasound device. Tumor volume was an estimate of (length × width^2)/2.[74,75] After 4 weeks, animals were euthanized by carbon dioxide asphyxiation, followed by cervical dislocation. Tumors were dissected and placed into liquid nitrogen for protein/RNA analysis or in 10% formalin for 48–75 h for histological analysis. The fixed samples were dehydrated 2 × 30 min in 50% ethanol, then 2 × 30 min in 70% ethanol and embedded into paraffin. To generate orthotopic tumors, mice (6–8 weeks old) were given buprenorphine 0.3 mg/kg (Temgesic, Schering-Plough

Nv, Brussels, Belgium) 30 min before inoculation. PC3 cells were inoculated into the ventral prostate of anesthetized mice.[76] Post-operationally, carprofen 5 mg/kg (Vet Rimadyl, Pfizer SA, Louvain-La-Neuve, Belgium) was administered subcutaneously every 24 h for three days.

Cell culture

Human PC3 cancer cell line was purchased from the American Type Culture Collection (ATCC, Manassas, VA, USA). UT-SCC-14 cell line was previously established at the University of Turku.[77] Cells were propagated in Dulbecco's Modified Eagle Medium/Nutrient Mixture F-12 (DMEM/F12) (D-18900, Sigma) supplemented with 10% Fetal Bovine Serum (FBS; S1810, Biowest) and 1% penicillin/streptomycin (15140-122, Gibco Life Technology). Cells were cultured at 37°C in a humidified 5% CO_2 incubator. For puromycin treatment, PC3 cells were seeded on a 6-well culture plate (657160, Greiner bio-one) and allowed to grow to attain 70-80% confluency, and then treated with translational inhibitor Puromycin (A1113803, ThermoFisher; 2.5 μg/mL in the complete medium) for 24 h to induce stress. After 24 h, cells were immunostained with anti-DDX4 antibody.

Organotypic 3D culture

For 3D culture experiments,[23] 800 UT-SCC-14 or PC3 cells were embedded between two layers of growth factor-induced Matrigel (356237, BD Biosciences) on IBIDI μ-plate angiogenesis 96-well plate (89646; Mediq 1700414). Wells were filled with 10 μL of 50% Matrigel/culture medium (1:1) and placed in a 37°C incubator for 30-60 min to polymerize. Cancer cells (~7000 cells) were seeded on top of the first layer and allowed to attach for 1–2 h in the 37°C incubator. The attached cells were covered with 20 μL s layer of Matrigel/culture medium (1:4), μ slides were humidified by 15 μL drops of sterile water or PBS and then placed in a 37°C incubator overnight. Wells were filled with 40 μL medium which was changed every second day.

Generation of *DDX4*-null cell lines

DDX4-null PC3 cells were generated *in vitro* with CRISPR/Cas9, via simultaneous expression of *S. pyogenes* Cas9 and two gRNAs, targeting different loci of exon 11 of *DDX4,* from a single plasmid vector,[78] with some modifications. The gRNAs were selected with a freeware package CRISPOR[79] (available at http://crispor.tefor.net), and assembled *in silico* into a single functional unit (Table S5A), which was purchased as a double-stranded DNA gene block (Cat.-No. 73431965, 73431966 IDT, USA) and ligated into pSpCas9 (BB)-2A-Puro plasmid[80]; PX459_V2.0, #62988 of Addgene repository). The ligation products were transformed into competent 10β *E. coli* (NEB) (Cat.-No. C3019H), according to the manufacturer's instructions. The transformed bacteria were kept overnight at +37°C on LB-agar plates with ampicillin (100 μg/mL). The emerged bacteria colonies were screened by genomic PCR[81] using primers #1–2 (Table S5B). Selected bacterial clones, exhibiting PCR products of the expected size on agarose gels, were further validated with Sanger sequencing (Macrogen Europe, the Netherlands) and used for targeting plasmid isolation (NucleoBond Xtra Maxi Plus; Macherey-Nagel). For targeting *DDX4,* PC3 or UT-SCC-14 cells (~300 000/well) were seeded into a 6-well culture plate (657160, Greinerbio-one) in 2 mL of DMEM/F12 supplemented with 10% Fetal Bovine Serum (FBS; S1810, Biowest), 1% penicillin/streptomycin (15140-122, Gibco Life Technology), and left in the incubator at +37°C overnight. The next day, the attached cells were transfected with the described *DDX4*-targeting plasmid (2.5 μg plasmid DNA per well), using Xfect reagent (Cat.-No. 631317 & 631318 Clontech Laboratories). After a recovery phase of 72 h, the cells were subjected to puromycin selection (A1113803, ThermoFisher; 1.25 μg/mL in the complete medium), which lasted approximately 7 days. Cells that survived puromycin treatment were allowed to expand for 2 weeks, then transferred into 96-well plates (Corning, 3367) by multiple serial dilution process to achieve growth of monoclonal cells (less than 1 cell per well) of well of 96-well plates. The growth of monoclonal cells was monitored under bright-field microscope. The resulting monoclonal populations were further expanded for about 2 weeks and then screened for *DDX4* mutations by PCR, as described.

PCR screening of *DDX4* mutations

To extract genomic DNA, cells were harvested by trypsinization, washed with PBS, resuspended in 50 μL of buffer L and 1 μL protease (Mouse Direct PCR kit, Cat.-No. B40015 Bimake), and incubated at +55°C for 45 min, then at +95°C for 5 min. The resulting DNA preps were used as templates for PCR reaction: 2 μL of the template, 200 nM of primers (#3–4, Table S5B), 25 μL of 2X MasterMix (Cat.-No. B40015 Bimake), and deionized water till 50 μL. The amplification was performed with the following cycle: 1) 5 min at +94°C, 2) 20 s at +94°C, 3) 30 s at +61.5°C, 4) 50 s at +72°C, back to step 2, for 34 × cycles overall, 5) final extension of 5 min at +72°C. PCR products were resolved on agarose gels (1.5% (w/v) agarose in 1xTBE buffer) and visualized with Midori Green Advance (Cat.-No. MG04 Nippon Genetics Europe) on Gel imaging system (Cat.- No. GP-07Led Nippon Genetics). Several samples with a clear size-shift of a sample's PCR product as compared to the size of WT control were further validated with Sanger sequencing (primers #3, 5–6; Table S5B). The two PC3 cell clones were found to harbor identical homozygous deletions of 103 base pairs in the targeted region of *DDX4*, leading to a frameshift and gene product loss (Figure S1A). UT-SCC-14 cell clones had slightly different gene rearrangements with homozygous deletion of 103 base pairs in null1 and 104 base pairs in null3 clone (Figures S1B and S1C).

2D proliferation assay

To monitor the proliferation of *DDX4*-null cancer cells, WT and *DDX4*-null cells were seeded at a density of 4000 cells/well in a 96-well plate (Corning, 3367). The growth profiles of UT-SCC-14 cells and PC3 cells were monitored for about 110 h and 70 h, respectively, using the Incucyte S3 live-cell analysis system (Sartorius, Göttingen, Germany).

Apoptosis assay

To analyze apoptosis in *DDX4*-null PC3 cells and WT PC3 cells, phosphatidylserine-based detection by Annexin V-FITC fluorescence probe binding assay was used. 250 000 cells (*DDX4*-null PC3 cells and WT PC3 cells) were seeded on a 6-well culture plate (657160, Greiner bio-one). Cultured cells were trypsinized in EDTA (about 10^5 or 10^6 cells/mL) and resuspended in ice-cold PBS. Cells were centrifuged 300 × g at 4°C for 5 min, then resuspended in 500 μL of 1X Annexin V binding buffer. 96 μL of cell samples were incubated in 1 μL Annexin V-FITC conjugate and 12.5 μL Propidium iodide (PI) solution for 10 min on ice in the dark incubation chamber. Stained live-cell suspensions were diluted to a final volume of 250 μL/assay with ice-cold, IX Annexin V binding buffer, and then analyzed by flow cytometry. Propidium iodide staining indicates cells that have lost membrane integrity, i.e., dead cells, while Annexin V-FITC stained living cells with the intact plasma membrane.

Quantitative phenotypic analysis of spheroids

DDX4-null PC3 and UT-SCC-14 spheroids were analyzed at different time points (day 5 and day 10) during their formation in 3D culture condition by using the Automated Image Analysis software (AMIDA). To achieve this, live-cell dye calcein (calcein AM) was mixed with cell culture medium (1:1000) and used to stain the growing spheroids in μ-plate angiogenesis 96-well plate (n = 10 wells for *DDX4*-null PC3 spheroids, n = 10 wells for WT PC3 spheroids; n = 10 wells for *DDX4*-null UT-SCC-14 spheroids, n = 10 wells for WT UT-SCC-14 spheroids) and incubated at 37°C for 1 h in the incubator. z stack Images were acquired with the spinning disk confocal microscope using a 5× objective. Acquired 3D images were converted to 2D images by maximum intensity projections using ImageJ 1.48 software version (National Institute of Health, USA). Representative images of spheroids were analyzed with AMIDA software, using the following settings: threshold value = 1, sensitivity = 0–20, smallest value (150–300 pixels), and the green channel "G" was selected to measure the calcein-stained spheroids. Morphometric parameters in AMIDA used for this study include: Area that defines the area of the segmented structures (in pixels) and the invasive processes or appendages (MaxApp) (in pixels) that defines the invasive property of the measured structures.[23] Results from the segmented structures were exported and analyzed using GraphPad Prism 9.0 version software.

Transient overexpression of DDX4

WT and *DDX4*-null PC3 cells were plated on 6-well culture plates. On the next day, *DDX4*-null PC3 cells were transfected with 2 μg of a plasmid encoding a human DDX4 fused with C-terminal EGFP (DDX4-EGFP, RG210628, OriGene) diluted in OPTIMEM 1(1X) (31985-062, Gibco Life Technology). As a control, we transfected 2 μg of a plasmid encoding EGFP alone. FuGENE HD (E2311/2, Promega) was used as a transfection reagent (ratio 2:1). After 24–48 h, transiently transfected cells were observed under the fluorescence EVOS Imaging System (Invitrogen) and then transfected cells were used for 3D-spheroid culture. Successful overexpression of DDX4-EGFP was validated by western blotting.

Primary antibodies

Primary antibodies used for immunostainings: DDX4 (Abcam, ab13840), αTubulin (Thermo Fisher Scientific, MS-581-P1), and Vimentin (GeneTex, GTX40346). Primary antibodies used for immunoprecipitation and western blotting: DDX4 (ProteinTech, 510421-1-AP), CDH1 (Cell signaling technology, 14472S), CDH2 (R&D systems, MAB13881) and CDH6 (Cell signaling technology, 48111S) were used for western blotting.

Immunofluorescence

Formalin-fixed and paraffin-embedded tissues were cut into sections (4 μm), mounted onto polylysine-coated slides, and deparaffinized: 3 × 5 min xylene, 2 × 10 min 100% ethanol, 2 × 10 min 96% ethanol, 2 × 10 min 70% ethanol, and 2 × 2 min Milli-Q water. Samples were subjected to antigen heat retrieval in citrate solution (10 mM sodium citrate, 0.05% Tween 20, pH 6.0) under 1 atm at 120°C for 20 min then allowed to cool down at room temperature (RT). Samples were washed 4 × 3 min with Milli-Q water and then with PBS. Cultured cells were fixed in 4% paraformaldehyde (PFA) solution at RT for 10 min, washed 3 × 5 min with PBS, and permeabilized with 0.2% Triton X- in PBS. Both tissue sections and cultured cells were blocked with 10% bovine serum albumin (BSA) in PBS containing 0.1% Triton X-100 (PBST) at RT in for 1 h before antibody incubations. For immunostaining of 3D-cultured spheroids, cells were fixed in 4% PFA at RT for 30 min and permeabilized in 0.7% Triton X- in blocking solution containing 20% horse serum in PBS at RT for 1 h. All samples were incubated in primary antibody diluted in respective blocking solutions at RT for 2 h or at +4°C overnight. After washing with PBST, samples were incubated with secondary antibodies (Alexa Flour 488/594, Life Technologies) diluted in respective blocking solutions at RT for 1–2 h. Nuclei were stained with DAPI (1:10000, D9542 Sigma-Aldrich, 5 mg/mL stock), and samples were either mounted with ProLong Diamond Antifade Mountant (P3690, Life Technologies) (tissue sections and cultured cells), or left in PBS for imaging (3D-cultured spheroids). 3i spinning disk confocal microscope, objective 100× 1.4 Oil (Intelligent Imaging Innovations) was used to acquire z stack images which were then processed with 3i SlideBook version 6

(Intelligent Imaging Innovations, USA) and ImageJ 1.48 software version (National Institute of Health, USA).[66] ImageJ software was used for generating maximum intensity projections from z stack images and background subtraction to remove noise.

Immunohistochemistry and scoring

Tissue sections were rehydrated by incubating in 3 × 5 min in xylene, 2 × 5 min in 100% Ethanol, 2 × 5 min in 96% Ethanol, 2 × 5 min in 70% Ethanol, then 5 min in distilled water. Samples were subjected to antigen heat retrieval in citrate solution (10 mM sodium citrate, 0.05% Tween 20, pH 6.0) under 1 atm at 120°C for 20 min, then allowed to cool down at RT for 2 h. Samples were washed with 0.05% Tween 20 in PBS solution (pH adjusted to 7.4 with HCl). To prevent non-specific binding, samples were incubated in a blocking solution containing 10% Bovine Serum Albumin (BSA) diluted in 0.05% Tween 20 in PBS solution (PBST) at RT in a humid chamber for 1 h, followed by primary antibody incubation (diluted in 10% BSA, PBST) at +4°C overnight. Samples were washed 2 × 5 min in PBST, followed by incubation with 1% hydrogen peroxide (H_2O_2 diluted in PBST) at RT for 20 min to block endogenous peroxidase reaction. Samples were incubated in secondary antibody (diluted in 10% BSA, PBST) for 30 min at RT, washed 2 × 5 min in PBST, and incubated with DAB kit solution according to manufacturer's instructions (K3468, DAKO North America, USA) and counterstained with Mayer's Hematoxylin solution (01820, Meyers HTX Plus). Samples were washed for 5 min in distilled water to avoid excess Hematoxylin staining, and dehydrated as follows: 2 × 5 min in 70% Ethanol, 2 × 5 min in 96% Ethanol, 2 × 5 min in absolute Ethanol, then 3 × 5 min in Xylene. Samples were mounted using Pertex (00801, Mounting Medium Pertex® Histolab). Mounted samples were allowed to solidify at RT overnight. Images were acquired with Pannoramic P1000 (3DHISTECH). Staining of DDX4 in human cancer samples was scored semi-quantitatively as negative, low and high expression. The cancer samples were evaluated independently by two pathologists blinded to the patient outcome.

Immunoprecipitation

To investigate DDX4-interacting partners in PC3 tumors, two PC3 xenograft tumors of 0.7 g were homogenized with Tissue-Lyser LT (69980, Qiagen) homogenizer in isotonic non-denaturing lysis buffer (50 mM Tris-HCl, pH 8.0, 150 mM NaCl, 5 mM EDTA, 1% Triton X-100, IX complete™ Mini Protease Inhibitor Cocktail, 0.2 mM PMSF and 1 mM DDT). Lysed cells were centrifuged at full speed (17000 × g) at +4°C for 20 min. The supernatant fraction of the lysed tumor sample was first precleared with 15 μL of washed Dynabeads Protein G (10446293, Invitrogen), then the precleared lysate sample was subjected to immunoprecipitation using beads coupled with 4 μg of anti-DDX4 rabbit polyclonal antibody (51042-1-AP, ProteinTech) and negative control rabbit IgG. The beads-antibody-antigen complexes were allowed to incubate on a vertical rotator at +4°C overnight, then washed three times with 1 mL of the lysis buffer. These complexes were used for mass spectrometry and western blotting.

Mass spectrometry

Samples for mass spectrometry analysis (antibody-antigen-beads complexes) were washed 3 × 1 mL of 50 mM Tris pH 8.0, digested and analyzed at the Turku Proteomics Facility of the Turku Bioscience using LC-ESI-MS/MS (2X Q Exactive HF Mass Spectrometer).

Western blotting

To analyze protein expression in tumor xenograft samples, Pierce BCA protein assay kit (23227, Life Technologies) was used to determine protein concentrations and absorbance measured with Victor™X4 plate reader (2030-0050, PerkinElmer). Protein lysates of equal amounts were diluted with Laemmli buffer, and heated at 95°C for 5 min. The immunoprecipitated protein complexes were eluted in Laemmli buffer by heating at 95°C for 5 min. Proteins were separated by 4–20% polyacrylamide gel electrophoresis (456-1094, Mini-PROTEAN®) using the settings: 100 V, 400 mA and 110 min. Proteins were then transferred onto PVDF membrane (10600023, RPN303F, Amersham™), with settings 90 V, 400 mA for 1 h at +4°C. To prevent non-specific binding, the membrane was incubated in a blocking solution (5% skimmed milk in PBST) at RT for 1 h, followed by the incubation with a primary antibody diluted in PBST at +4°C overnight. The next day, membranes were washed 3 × 15 min with PBST, incubated in secondary antibody (Horseradish Peroxide-conjugated anti-rabbit or anti-mouse IgG antibody (Cell signaling technologies) then washed again 3 × 15 min in PBST. The signal was detected with Western Lightening ECL pro (Ne11200IEA, PerkinElmer) and LAS4000 (Fujifilm). Images were saved as 16-bit TIFF files and processed with Adobe Photoshop Creative Suite 6.

RNA extraction and sequencing

Total RNA was isolated from cells and tumors using TRIsure (BIO-38033, Meridian Bioscience) according to the manufacturer's instructions. To remove any DNA contamination, DNase I (AMPD1, Sigma-Aldrich) was used. The quality of total RNA was ensured with Advanced Analytical Fragment Analyzer. Sample concentration was measured with Qubit® Fluorometric Quantitation, Life Technologies. Libraries were prepared using the Illumina TruSeq® Stranded mRNA kit (part#15031047). Small RNA libraries were prepared using the Qiagen QIAseq miRNA Library Kit. After confirming the high quality of the libraries with Advanced Fragment Analyzer and Qubit® Fluorometric Quantitation, the libraries were sequenced with Illumina HiSeq 2500 instrument. The quality control, library preparation and sequencing were carried out at the Finnish Functional Genomics Center (FFGC), Turku Bioscience, Finland.

mRNA-seq analysis

The quality of raw data were evaluated by FastQC (v0.11.9). The adapter and low-quality nucleotides were cut off from raw data by Trimmomatic (v0.39).[67] The clean data next were mapped to the reference human genome (GRCh37) by using STAR (v2.7.10a).[68] The read counts were calculated by featureCounts (v2.0.3).[69] Then we performed differential expression analysis from raw counts of protein-coding genes using the DESeq2 package (v1.40.2) in R.[70] Only the genes with minimal 10 counts across all samples were kept for the differential expression analysis. The *P*-adjusted value ≤ 0.05 and $|\log2foldchange| \geq 1$ were used for further analysis. Tumor suppressor genes were downloaded from https://bioinfo.uth.edu/TSGene/to study the expression level of these genes in *DDX4*-null and WT PC3 tumors. rMATS (v4.1.2) was used to analyze alternative splicing events based on the BAM files.[71] The Percent Spliced In (PSI) levels were calculated between the *DDX4*-null and WT PC3 cells by rMATS. The significant alternative splicing events were defined as FDR ≤ 0.05 and $|\Delta PSI| \geq 0.1$. The GO enrichment analysis of differentially expressed genes and alternatively spliced genes were done using the topGO package (v2.52.0) in R.

Small RNA-seq analysis

Fastq files were first screened by FastQC (v0.11.9) to assess the quality of the reads (http://www.bioinformatics.babraham.ac.uk/projects/fastqc/). For miRNA analysis, reads ranging beyond 19–40 nt and of low quality were discarded, and the adapters were trimmed off using cutadapt (DOI: https://doi.org/10.14806/ej.17.1.200) (v3.5). SPORTS 1.1[72] was used to map the reads to the human genome (Hg38) and allocate the reads to miRBase (v22) using the software's default settings. For piRNA analysis, reads ranging beyond 23–35 nt and of low quality were discarded, and the adapters were trimmed off using cutadapt. Hisat2[73] was used to map the reads to the human genome (Hg38), then reads mapping to tRNA or rRNA locations were discarded and the remaining reads were mapped to the previously annotated 180 piRNA clusters[32] using featureCounts (v2.0.0).

RT-qPCR

To validate gene expression based on the RNA-seq results, total RNA was isolated from three biological replicate samples of tumors and cells as described above. 1 μg of the total RNA was used for cDNA synthesis and qPCR was performed using SensiFAST cDNA Synthesis Kit (BIO-65054, Meridian Bioscience) and DyNAmo Flash SYBR Green qPCR Kit (F415L, Thermo Scientific) according to the manufacturers' instructions. qPCR samples were run on CFX384 Real-Time PCR System (Bio-Rad) with the following settings: initial denaturation 95°C for 7 min, and subsequently for 40 cycles, 95°C for 10 s, 60°C for 15 s, 72°C for 10 s, followed by final elongation at 72°C for 10 min. The PCR products were run on 1.5% agarose gel and the amplified products were visualized using Midori Green Advance DNA Stain (MG04, Nippon Genetics). The primers used for qPCR were ordered from Integrated DNA Technologies and are listed in Table S5C. Fold change in gene expression was calculated using *hRPL19* as a reference gene and data analyzed using GraphPad Prism 9.0.

QUANTIFICATION AND STATISTICAL ANALYSIS

For the analysis of gene expression and cell, spheroid and tumor properties, data were compared using the Mann-Whitney U test, 2-tailed using GraphPad Prism (version 9.0). Statistical significance was set at *p* value less than 0.05. Details on the statistical method used, sample size (n) and replicates are described in the figure legends and the method section. For statistical analysis of DDX4-granules in human cancer samples, low and high expression were combined as positive. The association between two categorical variables was analyzed using Fisher's exact test. PSA mean levels between DDX4 categories were compared with a two-sample t test. Log transformation was used for PSA to fulfill assumptions for the test. The association of DDX4-granules for survival and progression-free survival time (Figures 7A and 7B) was evaluated with a log rank test together with the Kaplan-Meier curve, continued with Cox's proportional hazard model. The significance level of 0.05 (Two-tailed *t* test) was used. The data analysis was generated using SAS software, version 9.4 of the SAS system for Windows (SAS Institute Inc., Cary, NC, USA) or GraphPad Prism (version 9.0).